Cellular and Molecular Life Sciences (2025) 82:264
https://doi.org/10.1007/s00018-025-05783-w

ORIGINAL ARTICLE

Circadian ontogenetic metabolomics atlas: an interactive resource with insights from rat plasma, tissues, and feces

Lucie Rudl Kulhava[1] · Pavel Houdek[1] · Michaela Novakova[1] · Jiri Hricko[1] · Michaela Paucova[1] · Ondrej Kuda[1] · Martin Sladek[1] · Oliver Fiehn[2] · Alena Sumova[1] · Tomas Cajka[1]

Received: 3 February 2025 / Revised: 14 May 2025 / Accepted: 2 June 2025

Abstract

Circadian rhythms regulate key physiological processes through clock genes in central and peripheral tissues. While circadian gene expression during development has been well studied, the temporal dynamics of metabolism across tissues remain less understood. Here, we present the Circadian Ontogenetic Metabolomics Atlas (COMA), which maps circadian metabolic rhythms across 16 rat anatomical structures. The brain (suprachiasmatic nuclei, medial prefrontal cortex) and periphery (liver, plasma) span developmental stages from embryonic E19 to postnatal P2, P10, P20, and P28. Fecal samples include all four postnatal stages, while additional peripheral tissues were analyzed at P20 and P28. Using a multiplatform liquid chromatography–mass spectrometry approach, we annotated 851 metabolites from 1610 samples. We identified distinct circadian shifts, particularly during the transition from nursing to solid food intake (P10–P20), with an average of 24% of metabolites exhibiting circadian oscillations across sample types, as determined by JTK_CYCLE. Our study also underscores the importance of standardized sampling, as metabolite intensities fluctuate with both circadian rhythms and development. COMA serves as an open-access resource (https://coma.metabolomics.fgu.cas.cz) for exploring circadian metabolic regulation and its role in developmental biology.

Graphical abstract

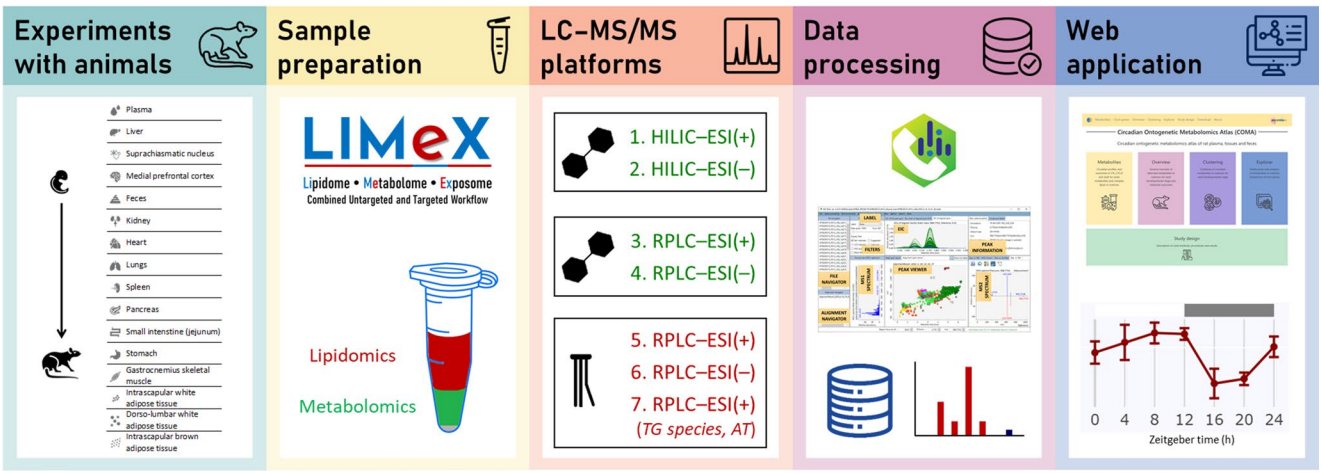

Keywords Metabolomics · Lipidomics · Circadian rhythm · Atlas · Resource

Lucie Rudl Kulhava, Pavel Houdek, and Michaela Novakova contributed equally to this work.

Alena Sumova and Tomas Cajka are Senior authors.

Extended author information available on the last page of the article

Published online: 28 June 2025

Introduction

The circadian rhythm, an approximately 24-hour physiological cycle, is ubiquitous across many organisms [1–3]. In mammals, it is orchestrated by a complex system involving a central clock located in the suprachiasmatic nuclei (SCN) of the hypothalamus, along with peripheral clocks distributed across neural structures and within peripheral tissues and organs [4–6]. The development of these circadian clocks during the prenatal period depends on the intricate differentiation and maturation of specific anatomical structures [7]. For example, in rats, neurogenesis within the SCN begins around embryonic day (E)14 and continues until E17 [8, 9]. This neurogenic process originates from a specialized zone within the ventral diencephalic germinal epithelium, which is part of the periventricular cell group. Although neurogenesis is complete by E18, morphological maturation of SCN neurons continues progressively until postnatal day (P)10 [10, 11].

In adults, the circadian system is hierarchically organized, with the central clock synchronizing subordinate clocks throughout the body, which is crucial for adapting physiological functions to cyclic external conditions. This system undergoes substantial developmental changes, including shifts in its responsiveness to external cues [12]. During the prenatal period, maternal signals primarily entrain the developing clock, whereas postnatally, the light–dark cycle becomes the dominant zeitgeber. The central clock acquires its functional properties gradually through a programmed process [13, 14], eventually entraining peripheral clocks that exhibit autonomous rhythmicity at different developmental stages [15]. In early development, maternal feeding is a primary driver of peripheral clock entrainment. As development progresses, the central clock becomes fully functional and takes over this regulatory role [11].

Despite extensive research primarily focused on gene expression, the development of circadian rhythmicity remains a subject of ongoing exploration [16]. Recent findings suggest cellular coupling and tissue-wide synchronization of single-cell rhythms may not occur until late in embryogenesis [10]. Our research and others have provided evidence that, throughout development, the phase of clock gene expression rhythms in certain tissues gradually shifts until reaching the adult stage [17, 18]. However, despite these advances, studies on circadian rhythmicity at the metabolite level during development remain scarce. Although transcriptomics has illuminated a substantial portion of the genome regulated by the molecular clock, metabolomics has been limited by the lack of robust analytical platforms and bioinformatics tools

Nevertheless, in the past decade, it has been shown that chemical profiling of biological specimens using mass spectrometry-based metabolomics is valuable in revealing the influence of the circadian clock on both mouse and human metabolism [19–22]. The circadian metabolome has been mapped under various conditions, such as sleep deprivation [23–25], jet lag [26, 27], exercise [28, 29], genetic perturbation [30, 31], different states of neuronal excitability [32], aging [33–35], acute or chronic cold exposure [36, 37], and nutritional challenges [38–40]. Most of these studies have analyzed plasma or serum, given their accessibility and role as a critical link between peripheral tissues. Recently, mapping metabolite dynamics over 24 h in plasma and multiple tissues, including liver, muscle, medial prefrontal cortex (mPFC), SCN, sperm, white adipose tissue (WAT), and brown adipose tissue (BAT) in response to chow and high-fat diets has been reported to provide important temporal insights [38]. Similarly, another study profiled serum and several tissues (muscle, liver, hypothalamus, heart, WAT, and BAT) following acute exercise performed at different times of the day [28].

Compared to circadian gene expression profiles, comprehensive bioinformatics resources mapping the circadian metabolite profiles in humans, mice, and rats are rare. The CircadiOmics portal, originally developed for transcriptomic data, was recently expanded to include metabolomic data from various mouse tissues analyzed using a multiplatform liquid chromatography–mass spectrometry (LC–MS) approach [38]. This resource allows users to explore hundreds of metabolites with circadian regulation, facilitating hypothesis generation and validation. A few datasets are available for download as supplementary materials from published studies [38, 41]. While not explicitly focused on the circadian metabolome, some attempts have been made to create metabolome databases for multiple tissues [42, 43]. However, these studies relied on a single analytical platform, capturing only a subset of the metabolome. This underscores the insufficient data on the circadian metabolome characterizing diverse tissues, emphasizing the need for easily accessible and reusable resources for future studies, as we recently highlighted in our discussion of metabolomics atlases [44].

To address this gap, we aimed to create an interactive, open-access atlas focused on the ontogenetic development of rats. This resource provides comprehensive metabolomics data across plasma, multiple tissues, and feces using a multiplatform LC–MS approach. Furthermore, by sharing raw LC–MS instrumental files, we facilitate retrospective data mining, potentially leading to additional annotations for unknown metabolites through spectral library search or the discovery of novel metabolites.

Materials and methods

Experiments with animals

Three-month-old male and female Wistar: Han rats (Institute of Physiology of the Czech Academy of Sciences) were kept under a 12:12 h light–dark cycle (lights on at 06:00 a.m., designated Zeitgeber time 0) at 21 ±2 °C with free access to food and water. Overhead 40 W fluorescent tubes provided light, resulting in illumination levels of 150 lx, varying based on cage position in the animal room. Female rats were mated with males, and those with positive sperm in vaginal smears were individually housed.

Fetuses were collected from the first group at embryonic day E19, while other groups were studied for postnatal development. After delivery on postnatal day 0 (P0), dams and their pups were maintained under a 12:12 h light–dark cycle, with the pups undisturbed and raised by their mother during lactation (P0–P20) on a standard diet (pellets). To collect the samples during the 24-hour cycle, fetuses were killed by rapid decapitation, and pups were euthanized at P2, P10, P20, and P28 with an overdose of thiopental (50 mg/kg, i.p.). Tissues (SCN, mPFC, liver) and plasma were collected for all five developmental stages. Feces were collected for P2, P10, P20, and P28 stages. For the P20 and P28 stages, additional tissues (kidney, heart, lungs, spleen, pancreas, small intestine (jejunum), stomach, gastrocnemius skeletal muscle, intrascapular WAT (isWAT), dorso-lumbar WAT (dlWAT), and intrascapular BAT (iBAT)) were collected. All samples were collected at Zeitgeber times 0, 4, 8, 12, 16, 20, and 24 h, each with five replicates. Samples for LC–MS were promptly stored at −80 °C until further processing and analysis, with plasma prepared from abdominal/thoracic blood using EDTA collection tubes. For the reverse transcription-quantitative polymerase chain reaction (RT qPCR) method, dlWAT samples were immersed in RNAlater (Merck), pancreas samples were immediately homogenized using ceramic beads in RNA isolation buffer (GenElute Total RNA kit, Merck), and whole brains were frozen in dry ice before storage at −80 °C. Brains were sectioned on cryocut, and SCN samples were dissected using laser-capture microdissection as described previously [45].

LC–MS-based metabolomics

For the sample extraction, a biphasic solvent system of methanol, methyl *tert*-butyl ether, and water was used to isolate complex lipids and polar metabolites. Six different LC–MS platforms [46] were used for profiling plasma, non-fat tissues, and feces with optimized conditions described before [47]: (1) hydrophilic interaction chromatography (HILIC) metabolomics in positive electrospray ionization mode (ESI(+)), (2) HILIC metabolomics in negative electrospray ionization mode (ESI(−)), (3) reversed-phase liquid chromatography (RPLC) metabolomics in ESI(+), (4) RPLC metabolomics in ESI(−), (5) RPLC lipidomics in ESI(+), and (6) RPLC lipidomics ESI(−), and (7) additional RPLC lipidomics analysis in ESI(+) on adipose tissues to detect abundant triacylglycerols.

Details about the sample extraction methods for each matrix, LC–MS analysis conditions, enhanced MS/MS spectra acquisition for metabolite annotation, quality control procedures, and LC–MS data processing are provided in the Supplemental Information. A list of annotated metabolites can be found in Table S1.

RT qPCR

The RT qPCR method was used to detect *Per1*, *Per2*, *Nr1d1/Rev-Erbα*, *Nfil3/E4bp4*, *Dbp*, *Cry1*, and *Bmal1* mRNA levels in selected tissues (3–5 replicates × group × time point). First, RNA was isolated using GenElute Total RNA kit (Merck, peripheral tissues) or RNeasy Micro kit (Qiagen, SCN), up to 0.5 µg was then reverse-transcribed using a High Capacity cDNA RT Kit (ThermoFisher). Diluted cDNA was then amplified on LightCycler480 (Roche) using SYBR Select qPCR Master Mix (ThermoFisher) as described previously [45, 48–50]. Liver samples were analyzed previously [18] and are included in the COMA dataset for convenience.

Statistical analysis and data visualization

JTK_CYCLE, designed to identify and characterize cycling variables in large datasets, was used [51]. The metabolomics data were $\log_{10}$ transformed and median normalized, followed by running the R script JTK_CYCLE v.3 with parameters: timepoints = 7, reps = 5, periods = 6, interval = 4. Metabolites with permutation-based *p*-values (*ADJ.P*) < 0.05 were considered statistically significant [41]. Reported *p*-values (*ADJ.P*) are, by default, Bonferroni-adjusted for multiple testing [51]. For "Outlier-free" analysis, data were $\log_{10}$ transformed, and for each group of 5 biological replicates, data points outside ±4 times the median absolute deviation were considered outliers and removed. For clustering analysis, data were $\log_{10}$ transformed and *z*-score normalized. For statistically significant metabolites (JTK_CYCLE, $p < 0.05$), the profiles were fitted to one of the six key clusters, with each graph displaying the number of metabolites in the cluster and their average Pearson correlation coefficient. Data from RT qPCR as relative expression were not further normalized.

Differential RhythmicitY analysis in R (*dryR*), developed to analyze rhythmicity in datasets comprising several conditions, was also used [52]. The metabolomics data were $\log_{10}$ transformed and median normalized, followed by execution of the R script dryR. The script (using f_24 function) was run separately for each matrix × developmental stage combination, reporting *p*-values corrected for multiple testing using the Benjamini–Hochberg method (*padj*). For the late developmental stages P20 and P28, the script was also run in parallel (using drylm function) to report rhythmicity models across these two conditions (Table S2), where model codes represent: 0 — no data available for calculation, 1 — non-rhythmic, 2 — loss of rhythm, 3 — gain of rhythm, 4 — unaltered rhythm, and 5 — altered rhythm. The distinction between models 4 and 5 is based on fitting the equation $y(t) = \mu + \alpha\cos(\omega t) + \beta\sin(\omega t)$, with identical α and β coefficients for model 4, and differing coefficients for model 5.

For multivariate analyses such as principal component analysis (PCA) and partial least squares-discriminant analysis (PLS-DA), the metabolomics data were $\log_{10}$ transformed and Pareto-scaled. For PCA, score and loading plots are provided, while for PLS-DA, variable importance in projection (VIP) scores are also reported. PLS-DA models were further assessed by 5-fold cross-validation, reporting the Q^2 performance measure (an estimate of the model's predictive ability) and permutation test results ($n = 1000$), yielding an empirical *p*-value.

The final dataset of polar metabolites, complex lipids, and clock genes for all samples was visualized in Plotly using a Python-based Flask web application. Circadian profiles are expressed as mean ± standard deviation for a particular group × time point.

Website implementation

Circadian Ontogenetic Metabolomics Atlas (COMA) is an interactive web application built using the Flask framework (https://flask.palletsprojects.com). The app uses an SQLite database (https://www.sqlite.org) accessed via Flask-SQL Alchemy for efficient data storage and management. The front end is styled with Bootstrap (https://getbootstrap.com), CSS (Cascading Style Sheets), and JavaScript. For visualizations, it uses Plotly (https://plotly.com/python), providing dynamic, interactive graphs. The app supports scientific analysis with machine learning algorithms from scikit-learn (https://scikit-learn.org), including PCA and PLS-DA, and integrates the JTK_CYCLE (https://sites.wustl.edu/hugheslab/jtk_cycle) and dryR algorithms (https://github.com/naef-lab/dryR) for detecting rhythmic components in the data.

Results

Building circadian ontogenetic metabolomics atlas (COMA)

We have studied the development of the circadian metabolome of rat brain, specifically in the SCN and mPFC, as well as in peripheral tissues such as the liver and plasma. This study spans five developmental stages, including embryonic E19 and postnatal stages P2, P10, P20, and P28 (see Fig. 1). Fecal samples were collected at all postnatal stages. For postnatal stages P20 and P28, additional tissues were collected, including the kidney, heart, lungs, spleen, pancreas, small intestine (jejunum), stomach, gastrocnemius skeletal muscle, isWAT, dlWAT, and iBAT. Sampling was conducted at Zeitgeber times 0, 4, 8, 12, 16, 20, and 24 h for all developmental stages. Following a well-established approach, clock gene analysis was also performed for SCN, liver, pancreas, and dlWAT.

As the construction of comprehensive mass spectrometry-based metabolomics and lipidomics atlases is an emerging field [44], we provide detailed information below and in the experimental section on sample preparation, instrumental platforms, data processing and curation, as well as quality control.

We analyzed 1610 study samples using untargeted LC–MS-based metabolomics platforms, accompanied by method blanks and quality control samples. To reduce extract complexity, we employed an "all-in-one" extraction approach (LIMeX) with methanol, methyl *tert*-butyl ether, and water [46, 47], resulting in two phases: the upper one containing nonpolar metabolites (complex lipids) and the bottom one mostly consisting of polar metabolites. The optimal plasma volume, tissue amount for extraction, collected aliquots, resuspension solvent volumes, and injection volumes were determined during a pilot study. The final injection volumes were confirmed using quality control samples before analyzing all study samples.

Each of these fractions underwent analysis under different separation conditions: HILIC for highly polar metabolites such as amino acids, biogenic amines, sugars, nucleotides, acylcarnitines, and sugar phosphates; RPLC for medium polar metabolites; and RPLC analysis of complex lipids. The optimal conditions of each LC–MS platform were based on our previously published methods [47], incorporating a high-throughput approach with each sample analyzed in less than 5 min [46].

LC–MS/MS raw data were processed using MS-DIAL software [53], including annotating polar metabolites (metabolomics workflow) and complex lipids (lipidomics workflow). All mass spectra underwent manual investigation, utilizing retention times and mass spectral information

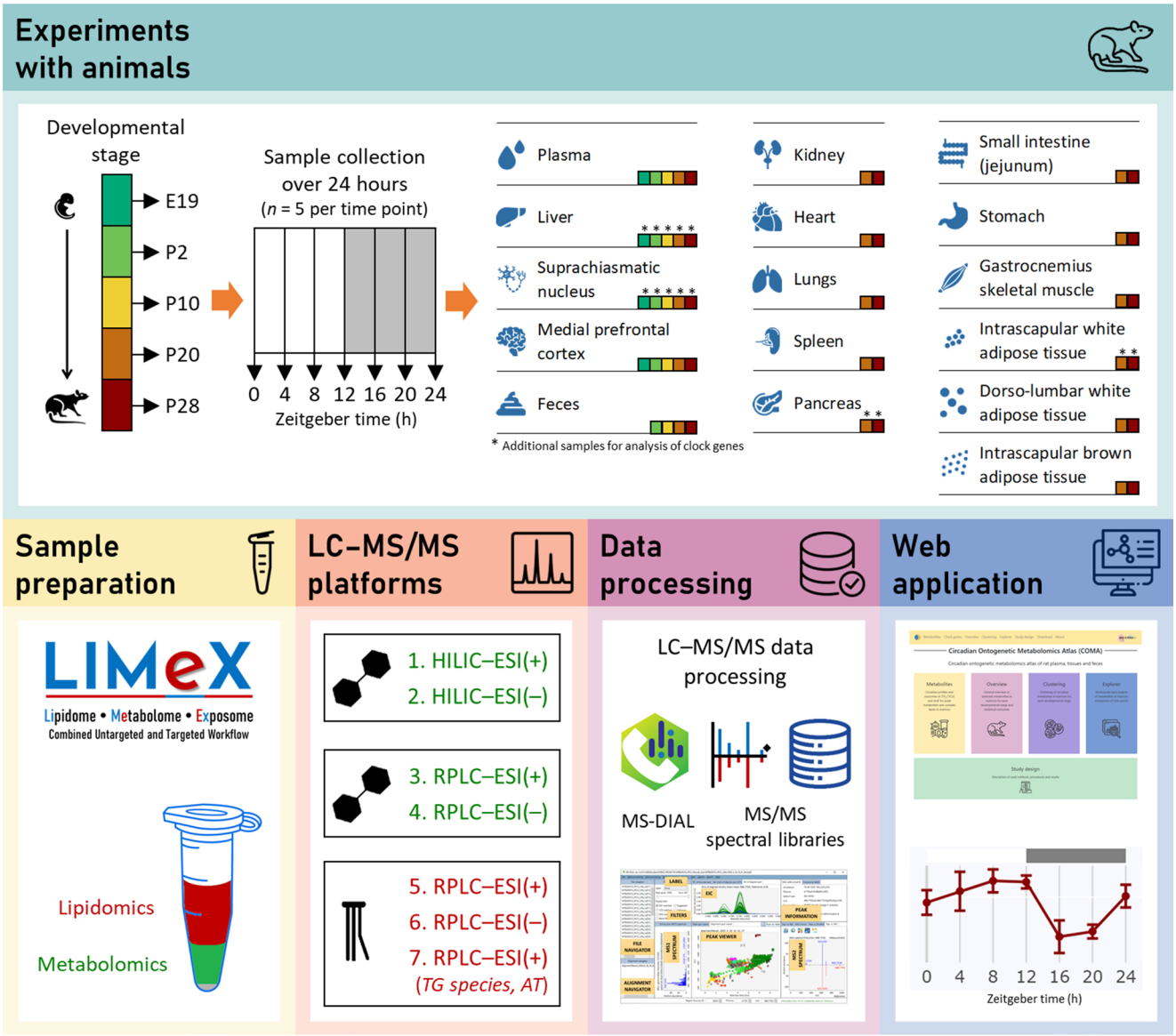

Fig. 1 Graphic illustration of the workflow toward building circadian ontogenetic metabolomics atlas of rat plasma, tissues, and feces

from MS1 and MS/MS libraries. To assess the precision of the overall analytical method, a superior quality control (SQC) sample was prepared by pooling QC samples from each matrix to reflect an aggregated metabolite composition. This SQC sample was aliquoted and repeatedly injected after every set of 35 samples (Fig. S1) and used to correct longitudinal signal drifts using locally estimated scatterplot smoothing (LOESS).

Overall analytical precision was evaluated through PCA of the total variance. As shown in the PCA score plot (Fig. S2), the tight clustering of SQC injections indicates minimal residual technical variability. In contrast, metabolomic and lipidomic profiles from different rat samples were more dispersed, with the first two principal components explaining over 42% of the total biological variance. Analysis of the SQC samples revealed that 84% of all annotated metabolites had excellent reproducibility, with relative standard deviations (RSD) below 10%. Furthermore, 99.2% of metabolites showed RSD values below 20%, underscoring the high quality and consistency of the dataset (Table S1). In total, 851 distinct metabolites were annotated and passed the quality control criteria (see Supplementary materials and methods). Coloring the PCA plots by matrices revealed clear biological differences among sample types. Fig. S3 shows samples from the SCN, mPFC, plasma, and feces formed distinct clusters, indicating pronounced metabolic differences in these compartments. In contrast, other tissue samples exhibited greater overlap, reflecting more subtle metabolic variation.

The annotated metabolites were used for subsequent statistical analyses, including JTK_CYCLE, a nonparametric algorithm for detecting rhythmic components in large datasets [51], and the recently introduced dryR algorithm, which assesses differential rhythmicity in time series data [52]. In addition, the metabolites were also included in multivariate analyses such as PCA and PLS-DA to provide an overview of the dataset [54].

As anticipated, complex lipids constituted the majority of reported metabolites (71%) due to their high endogenous content in various biological matrices. Main lipid classes included (lyso-)phosphatidylcholines (LPC, PC), (lyso-) phosphatidylethanolamines (LPE, PE), triacylglycerols (TG), free fatty acids (FA), acylcarnitines (CAR), phosphatidylserines (PS), phosphatidylinositols (PI), phosphatidylglycerols (PG), sphingomyelins (SM), ceramides (Cer), and diacylglycerols (DG). Organic acids, amino acids, modified amino acids, peptides, hydroxy acids, organic oxygen compounds, organoheterocyclic compounds, organic nitrogen compounds, nucleosides, nucleotides, and others were the main components of the polar metabolome.

Furthermore, the RT qPCR method [45, 48] was employed to detect mRNA levels of clock genes in the liver (*Per1*, *Per2*, *Rev-Erbα*, *Cry1*, *Bmal1*, *Clock*), SCN (*Per2*, *Rev-Erbα*, *Bmal1*, *Dbp*, *E4bp4*), pancreas, and dlWAT (*Per2*, *Rev-Erbα*) for further investigation of the rhythmicity during ontogenesis.

Web application

The dataset for this study comprises 1610 samples, each containing hundreds of annotated metabolites, including polar metabolites and complex lipids. Clock gene data are also available for four matrices: liver, SCN, pancreas, and dlWAT. Consequently, we developed the Circadian Ontogenetic Metabolomics Atlas (COMA), a web-based application for facilitating data visualization and interpretation (https://coma.metabolomics.fgu.cas.cz).

The atlas is structured into five main sections (Fig. 2A), offering circadian profiles and outcomes of JTK_CYCLE and dryR algorithms for polar metabolites and complex lipids in matrices, a general overview of detected metabolites in matrices for each developmental stage, clustering of circadian metabolites in matrices, multivariate data analysis of metabolites in matrices irrespective of time points, and study design.

The "Metabolites" section overviews all polar metabolites and complex lipids. Users can search for a specific metabolite by name, molecular formula, and InChIKey. Additional search options for complex lipids include the number of carbons and double bonds. The "Metabolomics" section is further divided into "Complex lipids" and "Polar metabolites." Profiles and outcomes of the JTK_CYCLE and dryR algorithms are displayed when selecting particular metabolites. Data are visualized for each developmental stage (E19, P2, P10, P20, and P28), along with the collected matrix and the calculated adjusted *p*-value (see an example of the amino acid citrulline) in Fig. 2-B. Oscillating metabolites ($p < 0.05$) are colored by default, while non-oscillating metabolites are gray. Users can adjust the *p*-value threshold according to their preferences. Results are available to the entire dataset without outlier detection (marked as the "Original" dataset) and after removing outliers based on the median value and the absolute deviation from the median, using upper and lower limits determined 4 times the median absolute deviation (marked as the "Outlier-free" dataset). Changes take effect after clicking the "Refresh plot" button, enabling users to compare the outcomes of both data pretreatment approaches.

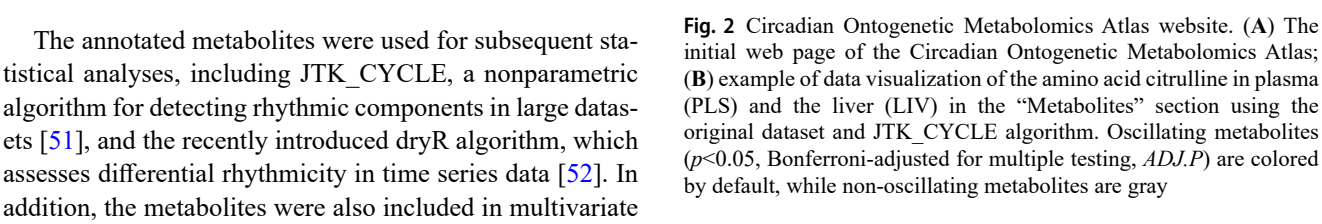

Fig. 2 Circadian Ontogenetic Metabolomics Atlas website. (**A**) The initial web page of the Circadian Ontogenetic Metabolomics Atlas; (**B**) example of data visualization of the amino acid citrulline in plasma (PLS) and the liver (LIV) in the "Metabolites" section using the original dataset and JTK_CYCLE algorithm. Oscillating metabolites ($p<0.05$, Bonferroni-adjusted for multiple testing, *ADJ.P*) are colored by default, while non-oscillating metabolites are gray

The "Overview" section provides a general overview of the composition of the analyzed matrices for each developmental stage. A sunburst graph visualizes hierarchical data in concentric circles, displaying the total number of unique annotated metabolites for each matrix and developmental stage, sorted into polar metabolites, complex lipids, and their respective classes. It also presents the total number of circadian metabolites identified using the JTK_CYCLE or dryR algorithms with a significance level of $p < 0.05$. Datasets without and with outlier detection were used, and metabolites with *p*-values above the threshold (0.05) are depicted in gray.

The "Clustering" section introduces categories for each matrix and developmental stage, combining JTK_CYCLE ($p < 0.05$) [51] and fuzzy c-means clustering [40, 55]. Six key categories indicate metabolite clusters with specific temporal dynamics based on the initial evaluation of each developmental stage and matrix, and considering typical clusters reported in the literature [40, 56]. The line width and opacity on each graph indicate the number of metabolites.

The "Explorer" section encompasses a statistical analysis of analyzed matrices, irrespective of Zeitgeber times. Matrices are categorized into digestive (liver, pancreas, stomach, small intestine), excretory (kidney, feces), respiratory (lungs), endocrine (spleen, isWAT, dlWAT, iBAT), muscular (gastrocnemius skeletal muscle), cardiovascular (plasma, heart), and nervous (SCN, mPFC) systems. Results of multivariate data analysis are presented using unsupervised PCA to visualize the first two principal components

A

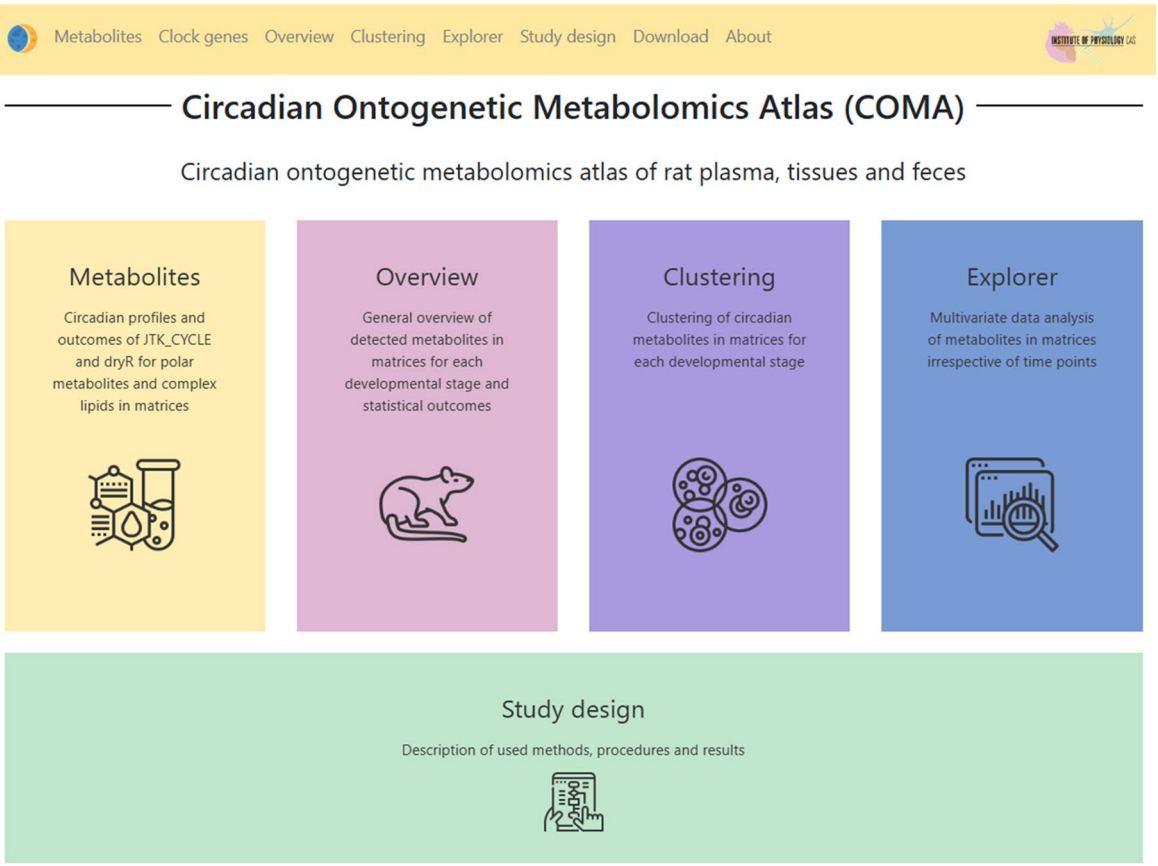
Metabolites
Clock genes
Overview
Clustering
Explorer
Study design
Download
About
Circadian Ontogenetic Metabolomics Atlas (COMA)
Circadian ontogenetic metabolomics atlas of rat plasma, tissues and feces
Metabolites
Circadian profiles and outcomes of JTK_CYCLE and dryR for polar metabolites and complex lipids in matrices
Overview
General overview of detected metabolites in matrices for each developmental stage and statistical outcomes
Clustering
Clustering of circadian metabolites in matrices for each developmental stage
Explorer
Multivariate data analysis of metabolites in matrices irrespective of time points
Study design
Description of used methods, procedures and results

B

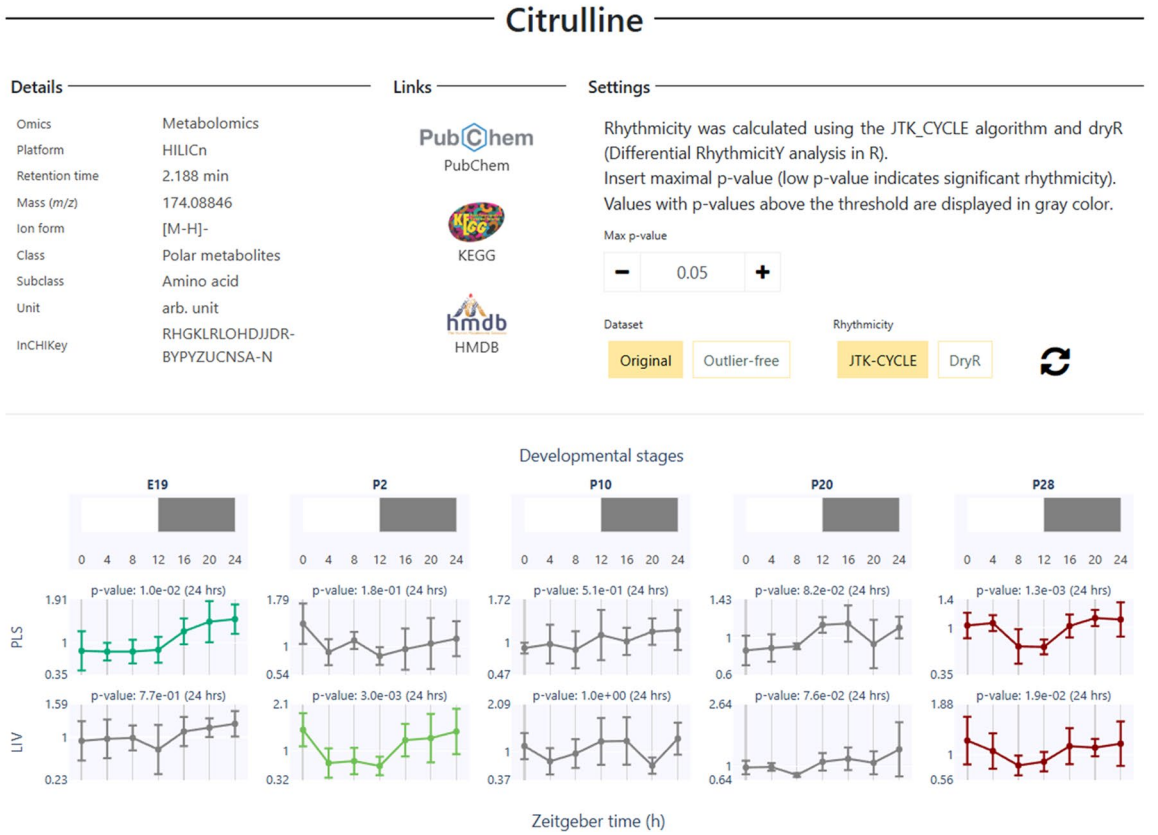
Citrulline
Details
Omics Metabolomics
Platform HILICn
Retention time 2.188 min
Mass (m/z) 174.08846
Ion form [M-H]-
Class Polar metabolites
Subclass Amino acid
Unit arb. unit
InCHIKey RHGKLRLOHDJJDR-BYPYZUCNSA-N
Links
PubChem
KEGG
HMDB
Settings
Rhythmicity was calculated using the JTK_CYCLE algorithm and dryR (Differential RhythmicitY analysis in R).
Insert maximal p-value (low p-value indicates significant rhythmicity).
Values with p-values above the threshold are displayed in gray color.
Max p-value
0.05
Dataset
Original
Outlier-free
Rhythmicity
JTK-CYCLE
DryR
Developmental stages
E19
P2
P10
P20
P28
PLS
LIV
p-value: 1.0e-02 (24 hrs)
p-value: 1.8e-01 (24 hrs)
p-value: 5.1e-01 (24 hrs)
p-value: 8.2e-02 (24 hrs)
p-value: 1.3e-03 (24 hrs)
p-value: 7.7e-01 (24 hrs)
p-value: 3.0e-03 (24 hrs)
p-value: 1.0e+00 (24 hrs)
p-value: 7.6e-02 (24 hrs)
p-value: 1.9e-02 (24 hrs)
Zeitgeber time (h)

through scores and loadings plots. Supervised PLS-DA is displayed with the first two components in scores and loadings plot formats, featuring a color-based gradient indicating VIP scores for all metabolites. In both PCA and PLS-DA, samples in score plots are color-coded based on the developmental stage. A sunburst graph offers a comprehensive overview of annotated metabolites in a specific matrix. Box plots are also presented for each metabolite sorted by VIP, and clicking on another metabolite updates the corresponding box plot.

The "Study design" section summarizes experimental conditions, including details about experiments involving animals, the methodology employed, and abbreviations utilized throughout the atlas.

Clock genes are accessible using the upper panel, and the data are visualized similarly to that of metabolites. This panel also includes a download section where users can download the whole data set, including metadata.

Exploring the circadian ontogenetic metabolomics atlas

In the following examples, we provide a snapshot of the results of the Circadian Ontogenetic Metabolomics Atlas, including the investigation of circadian metabolites in each matrix and developmental stage, the clustering of metabolites, and finally, general exploration using multivariate data analysis.

The results from applying the JTK_CYCLE and dryR algorithms to identify and characterize cycling metabolites are shown in Fig. 3. The figure provides an overview of the percentage of circadian metabolites, defined as those with adjusted *p*-values (< 0.05; *ADJ.P* for JTK_CYCLE and *padj* for dryR) and a period (PER) of 24 h. Across matrices and developmental stages, the average percentage of oscillating metabolites was approximately 24% with JTK_CYCLE and 12% with dryR. Stomach tissue, SCN, and mPFC were identified with the lowest number of circadian metabolites, while dlWAT, isWAT, liver, and plasma had the highest number of circadian metabolites.

An example of the clustering of metabolites is provided in Fig. 4 on plasma samples for all five developmental stages, illustrating commonalities in their temporal dynamics. These categories of the clusters can be characterized as follows:

(A) Metabolites with a gradual increase during the daytime inactive phase, reaching a maximum of around 4–8 h, followed by a decrease with a minimum at 16–20 h;
(B) Metabolites with a gradual decrease during the daytime inactive phase, reaching a minimum of around 4–8 h, followed by an increase with a maximum at 16–20 h;

Fig. 3 Overview of the total number and percentage of circadian metabolites by matrix and developmental stage. The original dataset (without outlier analysis) was processed using (**A**) JTK_CYCLE, considering metabolites with Bonferroni-adjusted $p<0.05$ (*ADJ.P*) as statistically significant, and (**B**) dryR, considering metabolites with Benjamini–Hochberg-adjusted $p<0.05$ (*padj*) as statistically significant

(C) Metabolites exhibiting a gradual increase during the daytime inactive phase and a rapid decrease when feeding starts at night;
(D) Metabolites rapidly decreasing at the onset of the inactive phase, rising upon feeding until plateauing in the middle of the night;
(E) Metabolites exhibiting a gradual increase during the daytime inactive phase and a rapid decrease when feeding starts at night;
(F) Metabolites with a shallower decline during the inactive phase, a temporary decrease at the onset of feeding, followed by an increase 2 h after feeding begins.

For the E19 developmental stage, cluster A contained the highest number of metabolites (32%) within the clusters, whereas for P2 and P10, metabolites in cluster F dominated (45% and 65%, respectively). In the late developmental stage P20, cluster B exhibited the highest number of metabolites (42%), while metabolites in cluster A dominated the developmental stage P28 (40%). These data suggest that metabolite profiles undergo significant changes during ontogenesis.

Since the lipidome constituted the largest proportion of reported metabolites, we also implemented downloaded lists of lipids formatted for a recently introduced web-based tool called Lipid Over-Representation Analysis (LORA) [57]. LORA determines whether a priori-defined set of lipids is more present (over-represented) in a subset of lipids than would be expected by chance. A list of query lipids can be downloaded from the "Cluster" section for each matrix and developmental stage. Additionally, the entire reference lipidome can be obtained from the "Download" section (lipidome_universe.csv) and uploaded to the LORA tool at https://lora.metabolomics.fgu.cas.cz. Fig. S4 illustrates an example of plasma at the P28 developmental stage for cluster A, revealing 127 statistically significant metabolites, most of which ($n = 120$) are complex lipids. The UpSet plot helps identify the main structural features of enriched lipids and highlights important lipids in a graphical representation, particularly TGs containing 10:0, 12:0, and 14:0 fatty acyl chains. Using the cardinality bar plot, the cluster with the highest term intersection size ($n = 18$) contained TGs with a 10:0 fatty acyl chain. The second cluster contained 14 lipid species with TGs containing a 12:0 fatty acyl chain.

Furthermore, the atlas can also be used for a more general audience using the "Explorer" function. Using PLS-DA

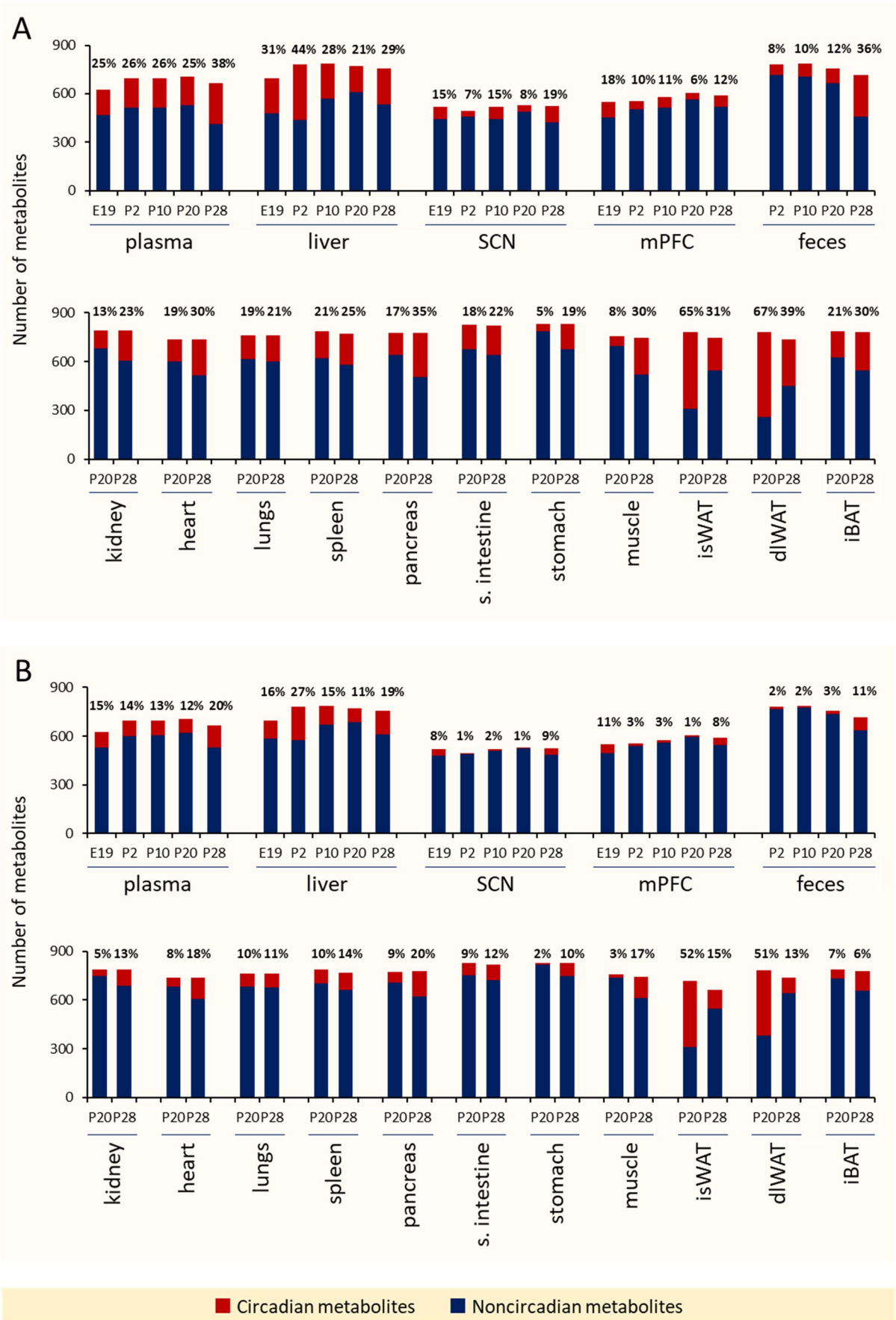
A
Number of metabolites
900
600
300
0
25% 26% 26% 25% 38%
31% 44% 28% 21% 29%
15% 7% 15% 8% 19%
18% 10% 11% 6% 12%
8% 10% 12% 36%
E19 P2 P10 P20 P28
P2 P10 P20 P28
plasma
liver
SCN
mPFC
feces
13% 23%
19% 30%
19% 21%
21% 25%
17% 35%
18% 22%
5% 19%
8% 30%
65% 31%
67% 39%
21% 30%
P20P28
kidney
heart
lungs
spleen
pancreas
s. intestine
stomach
muscle
isWAT
dlWAT
iBAT
B
Number of metabolites
15% 14% 13% 12% 20%
16% 27% 15% 11% 19%
8% 1% 2% 1% 9%
11% 3% 3% 1% 8%
2% 2% 3% 11%
plasma
liver
SCN
mPFC
feces
5% 13%
8% 18%
10% 11%
10% 14%
9% 20%
9% 12%
2% 10%
3% 17%
52% 15%
51% 13%
7% 6%
kidney
heart
lungs
spleen
pancreas
s. intestine
stomach
muscle
isWAT
dlWAT
iBAT
Circadian metabolites
Noncircadian metabolites

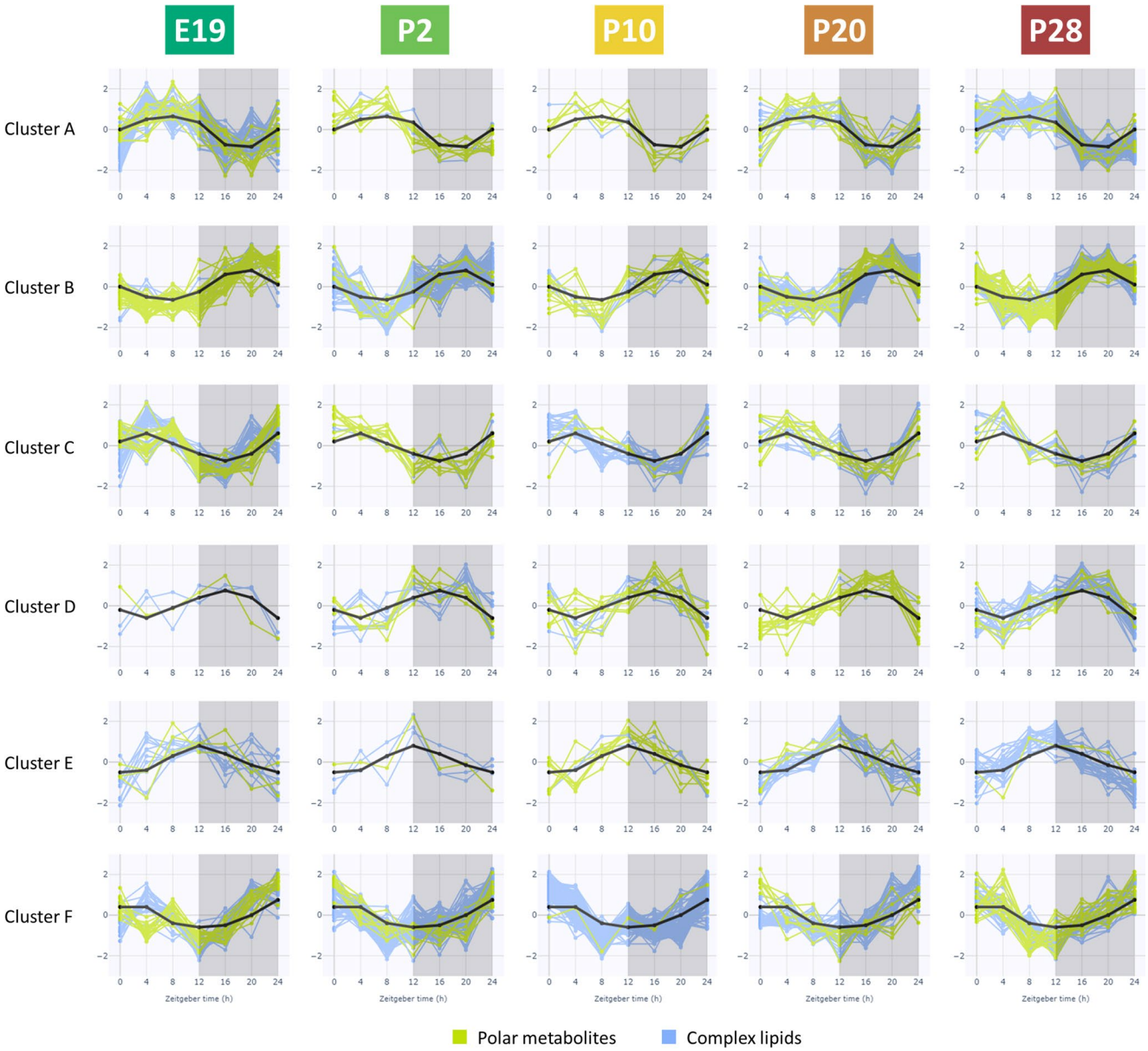

Fig. 4 Cluster analysis of plasma samples by developmental stage. Six clustering categories are shown. Only polar metabolites and complex lipids with significant circadian oscillation (JTK_CYCLE, *ADJ.P*<0.05) were included in the analysis

and VIP scores, it became apparent that distinct metabolites were characteristic of the analyzed matrices. For instance, in plasma, inosine (a nucleoside) dominated during the fetal E19 stage, continuously declining in postnatal stages. In the liver, glycocholic acid (a bile acid) was completely absent during fetal and early postnatal P2 and P10 stages and dominated in the P20 and P28 stages (Fig. 5A, B). In the SCN, the lipid PI 32:0 was also absent during the fetal and early postnatal P2 stage and increased over the P10, P20, and P28 stages (Fig. 5C). Similarly, HexCer 42:1;O2 was detected at higher levels in mPFC during postnatal P20/P28 stages (Fig. 5D). In feces, the vitamin riboflavin dominated during the early postnatal P2/P10 stages and was almost absent in the P20/P28 stages (Fig. 5E). These examples also show that the metabolome undergoes dramatic changes from the fetal to late postnatal developmental stages. For the rest of the matrices collected at the P20 and P28 postnatal stages, differences were observed in a way that a few metabolites occurred only in one developmental stage or differed in their intensities for most of them. These data also underscore the critical role of sampling time in metabolomics analyses, as the intensity of specific metabolites can vary significantly based on the time of collection and developmental stage. Metabolites are influenced by circadian rhythms, which govern biological processes and fluctuate throughout the day and night. This timing-dependent variation can impact the detection and quantification of metabolites,

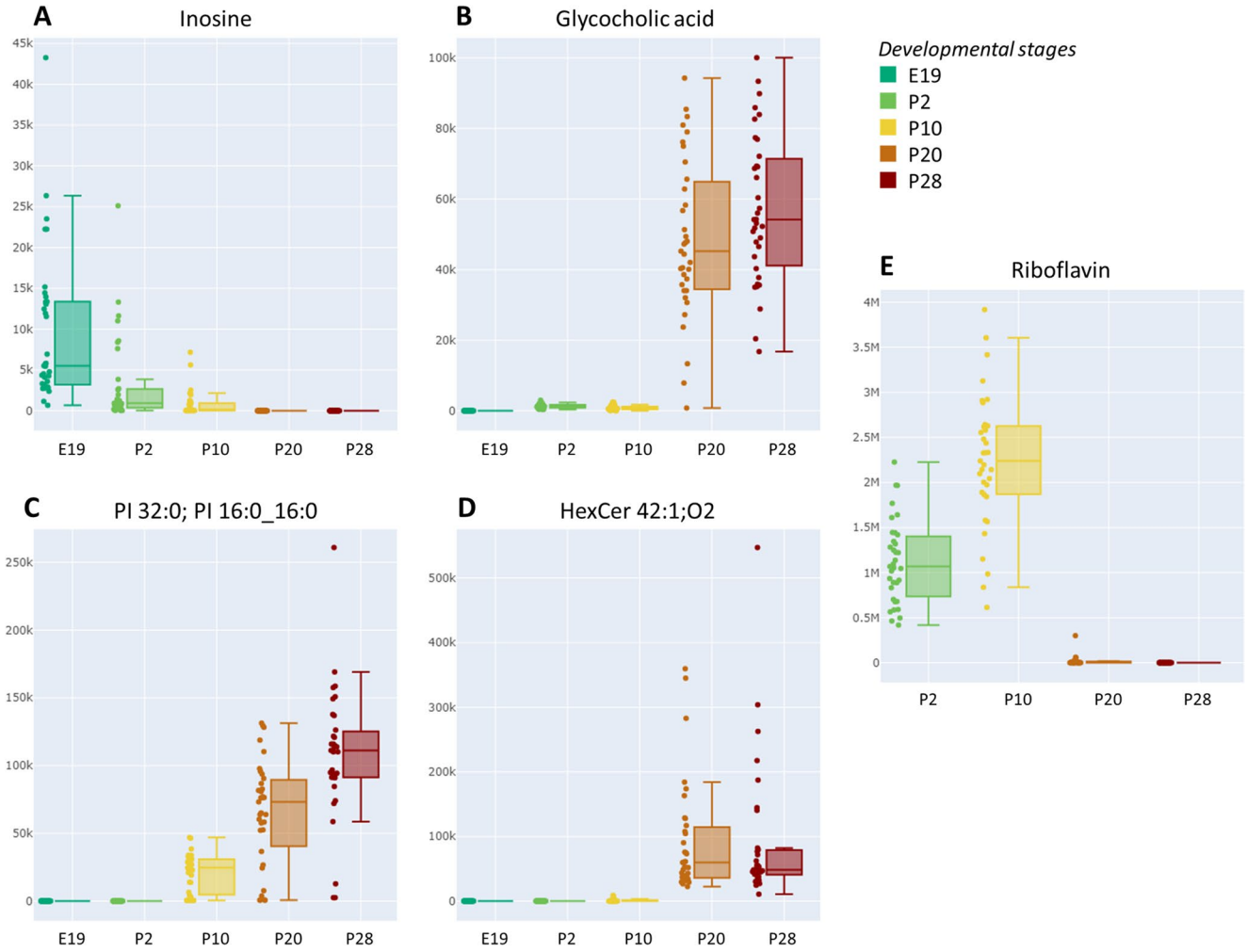

Fig. 5 Box plots for the most discriminating metabolites in (**A**) plasma, (**B**) liver, (**C**) SCN, (**D**) mPFC, and (**E**) feces at different developmental stages based on PLS-DA and VIP

potentially leading to biased or inaccurate interpretations if sampling is inconsistent. Using animals within the same developmental stage, or "age-matched" subjects, alongside standardized sampling times, is essential to minimize variability and improve sample comparability.

Users can also explore the analysis of clock genes. For instance, *Bmal1*, *Per2*, *Nr1d1*, and *Dbp*, in the SCN, revealed shallow rhythms at E19, followed by initiation at P2. Rhythms increased at P10, and high amplitude was observed at the P20 and P28 developmental stages (Fig. S5), as observed before in fetal E20 and early postnatal P1, P2 [58], and P10 [59] developmental stages, as well as in adult rats [11].

Potential for the discovery of novel metabolites

Hundreds of unique metabolites can usually be annotated while combining multiple platforms during untargeted metabolomics and lipidomics analyses. However, many more signals can be detected, characterized by retention time and *m/z* (i.e., molecular features) [60]. The raw LC–MS instrumental files provided with this atlas can be reprocessed, including updated MS/MS libraries, to increase the annotation rate further, or researchers can focus on the structural elucidation of unknown metabolites.

For example, we initially observed an unknown with a retention time of 2.2 min and *m/z* 188.1757 without any positive spectral match when using the combined MS/MS libraries during the HILIC platform in positive ion mode. Submitting MS1 isotopic ions and the MS/MS spectrum from MS-DIAL [53] to the MS-FINDER [61] software for structural elucidation provided over 100 possible unique structures. Since focusing on many structures would be challenging, we utilized the potential of hydrogen/deuterium exchange mass spectrometry (HDX-MS). Thus, for the HILIC–MS metabolomics platform, which uses acetonitrile/water (95:5) and water as mobile phases, both with ammonium formate and formic acid, water and

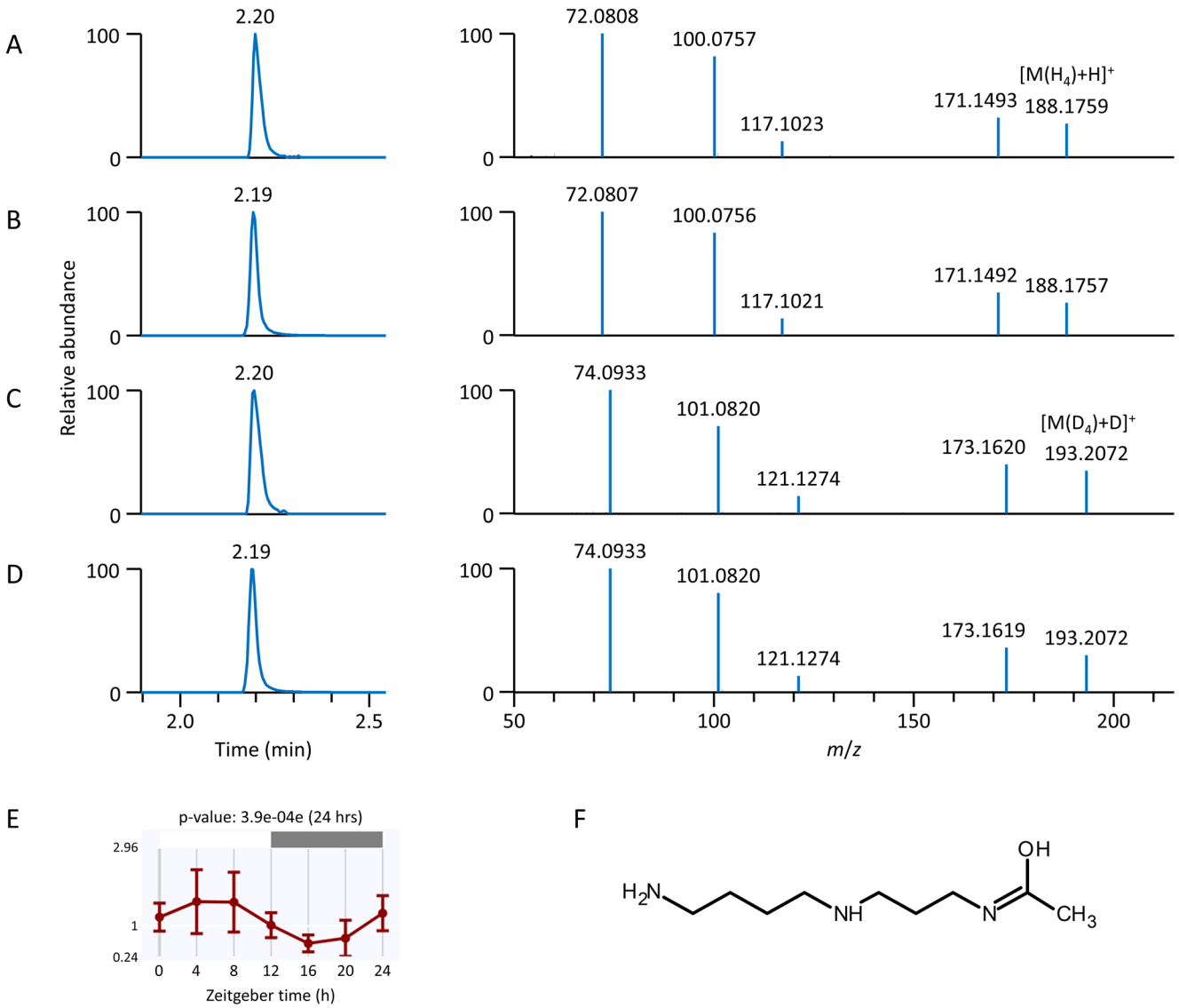

Fig. 6 Structure elucidation of an unknown metabolite. (A, B) Extracted ion chromatograms (EICs) and MS/MS spectra of N^1-acetylspermidine in (**A**) rat gastrocnemius skeletal muscle and (**B**) analytical standard analysis under conventional HILIC–MS with the EIC at *m/z* 188.1757 displayed corresponding to $[M(H_4)+H]^+$. (C, D) EICs and MS/MS spectra of N^1-acetylspermidine in (**C**) rat gastrocnemius skeletal muscle and (**D**) analytical standard analysis under HILIC–HDX-MS with the EIC at *m/z* 193.2071 displayed corresponding to $[M(D_4)+D]^+$. (**E**) Circadian rhythmicity of N^1-acetylspermidine in gastrocnemius skeletal muscle at the P28 developmental stage, calculated using JTK_CYCLE with a Bonferroni-adjusted *p*-value (*ADJ.P*). (**F**) Structure of N^1-acetylspermidine

mobile-phase modifiers were replaced by their deuterated forms (D_2O, ammonium formate-d_5, formic acid-d_2). This setup permitted complete hydrogen/deuterium exchange and an additional filter from hydrogen/deuterium exchange mass spectrometry (HDX-MS) [62], reducing the number of potential candidates to one-fifth due to four labile hydrogens in the molecule as determined by a mass spectrometer. The subsequent analysis of the standard of N^1-acetylspermidine confirmed the identity of this unknown based on retention time, MS1, and MS/MS spectra, including the number of exchangeable hydrogens in the parent ion and fragments (Fig. 6) when using unlabeled mobile-phase modifiers and labeled counterparts. Furthermore, N^1-acetylspermidine exhibited circadian rhythmicity in different tissues at late developmental stages (P20, P28), as shown in the example of gastrocnemius skeletal muscle (Fig. 6).

Discussion

Selection of matrices and developmental stages

We investigated the development of the circadian metabolome in the rat brain (SCN, mPFC) and periphery (liver,

plasma) across five different developmental stages. Furthermore, feces were studied at four developmental stages (P2, P10, P20, P28), while the other 11 tissues (kidney, heart, lung, spleen, pancreas, small intestine (jejunum), stomach, gastrocnemius skeletal muscle, isWAT, dlWAT, and iBAT) were examined at late developmental stages (P20, P28). As a well-established approach, clock gene expression was analyzed in the SCN, liver, pancreas, and ldWAT.

The SCN and mPFC were selected due to their significant developmental changes during both embryonic and postnatal stages. The SCN, as the central circadian clock, plays a crucial role in developing the circadian system [10]. The liver, where approximately 10% of the transcriptome exhibits rhythmic expression, regulates glucose, lipid, and nutrient homeostasis, as well as bile acid synthesis and metabolism. Plasma, acting as a vital link between peripheral tissues [63], was also included in the study. Feces were included because the circadian system influences various gastrointestinal processes and is influenced by feeding time [64].

Clocks, similar to those found in SCN neurons, are present in peripheral tissues [65–67]. For example, various renal functions exhibit circadian rhythms, such as renal plasma flow and glomerular filtration rate. Alterations in the circadian rhythm of renal functions are associated with developing hypertension, chronic kidney disease, renal fibrosis, and kidney stones [68]. Moreover, evidence indicates a close relationship between intrinsic circadian clocks and cardiovascular functions. Well-known circadian rhythms include diurnal changes in blood pressure and heart rate. Animal models and epidemiological studies provide strong evidence that the disruption of circadian rhythms is a significant risk factor for many cardiovascular diseases [69]. Circadian rhythms play an important role in regulating the digestive systems of many organisms. Cell proliferation, migration, differentiation, and even structure vary as a function of the time of day in various digestive organs (such as the liver, pancreas, and small intestine) and cell types, leading to regionally specific temporal variations in protein and gene expression [70, 71]. A link also exists between the circadian clock and rhythmic immune functions. The spleen, lymph nodes, and peritoneal macrophages contain an autonomously intrinsic circadian clockwork [72]. In mammals, pulmonary function follows day–night patterns. Hence, the molecular clock function in lung cells may function as a biomarker for disease severity and exacerbations or for evaluating the effectiveness of chronotherapy in disease management [73]. The cell-intrinsic clock machinery in skeletal muscle could be critical for whole-body metabolic homeostasis [74]. Last but not least, the circadian clock controls different aspects of lipid metabolism in WAT and BAT, including lipolysis, lipogenesis, and BAT thermogenesis [75].

The chosen developmental stages represent key milestones in rat development [10, 11]. At E19, neurogenesis is completed, although the morphological maturation of SCN neurons has not yet been concluded. In the early postnatal period (P2), substantial reorganization and functional specialization occur in the rat SCN, forming various cell subpopulations. By postnatal stage P10, the SCN clock is fully developed, while the pups' eyes remain closed, and they are still entirely dependent on maternal care. The period between P10 and P20/P28 marks a developmental phase during which pups gain sight, experience a gradual decline in breast milk intake, and initiate solid food consumption at night, influencing the phases of their peripheral clocks [76]. A comparison between postnatal stages P20 and P28 was included to generate evidence for arguments in favor of or against premature weaning, typically performed at P21. Some studies suggest that later stages might be more appropriate [77].

Experimental considerations

When interpreting circadian metabolomics data, it is essential to account for various experimental aspects that may influence the detection and characterization of rhythmic metabolites [78]. These variables include diet, feeding schedule, light–dark cycle, and sampling time [78]. For instance, Dyar et al. [38] demonstrated that, in mice, a chow diet maintained strong temporal coherence of metabolites within and across tissues, whereas a high-fat diet disrupted this coherence and rewired circadian metabolism. Additionally, under *ad libitum* (free-feeding) conditions, rodents (particularly nocturnal species like rats and mice) often engage in sporadic daytime feeding or "snacking" behavior, which can influence both metabolomic and transcriptomic profiles [52, 79].

Although laboratory conditions provide tight control of light and feeding, real-world factors like shift work and artificial lighting can significantly disrupt circadian rhythms, affecting metabolic oscillation amplitude, phase, and robustness [78]. Future studies incorporating dynamic environmental conditions or leveraging human cohort data with diverse lifestyle factors could enhance our understanding of how external cues influence circadian metabolic regulation.

In addition to experimental factors, statistical modeling also plays a crucial role. In our analysis, we applied the well-established JTK_CYCLE algorithm [51] alongside the recently introduced dryR model [52]. Across matrices and developmental stages, the average percentage of oscillating metabolites was approximately 24% with JTK_CYCLE and 12% with dryR. This two-fold difference can be attributed to the underlying assumptions and sensitivity of the respective methods. JTK_CYCLE is a nonparametric algorithm

optimized for detecting robust, sinusoidal rhythms with fixed periods (e.g., 24 h), making it particularly sensitive to clear, consistent oscillations. In contrast, dryR uses linear mixed-effects regression to model rhythmicity, accounting for amplitude and phase variability across conditions. This makes it more conservative and better suited to identifying context-specific or differential rhythmicity. Consequently, dryR may detect fewer circadian metabolites but potentially capture more biologically nuanced patterns. In JTK_CYCLE, adjusted *p*-values (*ADJ.P*) reflect multiple testing correction, with $ADJ.P < 0.05$ commonly used to define circadian regulation [38]. However, it is often useful to compare multiple *ADJ.P* thresholds and empirically assess the biological plausibility of rhythmic patterns [80].

The disparity in circadian detection between methods highlights how methodological choices can influence the interpretation of rhythmicity in high-dimensional omics datasets. Nonetheless, the percentage of circadian metabolites reported here aligns with recent findings from a mouse circadian metabolome atlas, which showed that 20–50% of metabolites across various tissues (SCN, mPFC, muscle, BAT, WAT, liver, sperm) and serum displayed 24-hour oscillations regardless of diet [38].

Developmentally, except for isWAT and dlWAT, the P20 stage exhibited fewer circadian metabolites than P28 across all matrices (Fig. 3**)**. Moreover, using the dryR model to assess rhythmicity across late developmental stages (P20 and P28) in parallel, we observed a loss of rhythm in approximately 12% of metabolites, a gain of rhythm in 13%, stable rhythmicity in 12%, and altered rhythmicity in 2% (Table S2). The transitional period between P20 and P28 encompasses physiological and behavioral changes associated with weaning, likely influencing tissue metabolite rhythmicity. At P20, pups are still partially reliant on maternal milk, whereas by P28, they are typically fully weaned and consuming solid chow, establishing circadian-regulated feeding behaviors more akin to adult patterns. For instance, using the "Explorer" function in COMA, we identified characteristic temporal profiles of plasma TGs containing short-chain saturated fatty acids. These TGs are synthesized *de novo* from maternal milk enriched in saturated fatty acids [81]. Their abundance peaks at P10, declines at P20, and drops to very low levels by P28, consistent with the weaning transition (Fig. S6**)**.

As noted, the metabolome shows dramatic changes from fetal to late postnatal stages, as highlighted by the most discriminating metabolites in PLS-DA and VIP (Fig. 5) through the "Explorer" function. Purine metabolites, such as inosine, hypoxanthine, and adenosine, progressively decline from E19 to P28 (Fig. S7). This decline likely reflects a shift from high purine turnover during rapid growth and nucleic acid synthesis to lower metabolic demands in more mature stages. These metabolites, associated with hypoxia and energetic stress, suggest a developmental maturation from rapid growth to homeostasis [82]. HexCer 42:1;O2 and related species (HexCer 40:1;O2 and HexCer 41:1;O2) increased markedly in the mPFC from E19 to P28 (Fig. 5D, Fig. S8), aligning with oligodendrocyte maturation and myelination. These glycosphingolipids support membrane structure and signaling, and their rise reflects growing myelin synthesis and membrane remodeling during postnatal cortical development [83]. Glycocholic acid, a glycine-conjugated primary bile acid, exhibited a marked increase in rat liver from early postnatal to weaning stages (Fig. 5B). This dramatic shift likely reflects the maturation of hepatic bile acid synthesis pathways and the onset of enterohepatic circulation, which become fully functional around weaning [84]. In the prenatal and early postnatal period (E19–P10), the fetal liver has limited bile acid production, and maternal supply dominates. By P20–P28, the weaning transition drives increased dietary fat intake, requiring enhanced bile acid secretion for digestion and absorption. Riboflavin levels in rat feces were high at early postnatal stages (P2 and P10) but declined sharply by P20 and were nearly undetectable at P28 (Fig. 5E). This likely reflects excess riboflavin from maternal milk, immature vitamin absorption, and limited microbial utilization in early life [85]. As the gut matures and diet shifts during weaning, fecal riboflavin levels decrease accordingly.

An open-access resource for circadian metabolomics

Understanding the circadian regulation of metabolism requires comprehensive datasets that capture metabolite rhythms across tissues and developmental stages. However, bioinformatics resources offering circadian metabolite profiles in animals remain limited, and detailed information on tissue-specific metabolite composition is scarce. Currently, the only available platform is the CircadiOmics web portal (https://circadiomics.igb.uci.edu), a repository and analytical tool for circadian omics data (transcriptomic, proteomic, and metabolomic) [86]. It includes metabolomics datasets primarily from mouse studies, covering plasma/serum and various tissues (e.g., brain, liver, muscle, adipose tissue) under different experimental conditions (e.g., chow vs. high-fat diet, exercise, wild-type vs. knockout models). While users can select datasets and request visualizations and statistical analyses (using BIO_CYCLE.2 and JTK_CYCLE), there is no comprehensive browser or complete list of metabolites for individual studies. Users must first download the metabolite list from the original publication, typically from supplementary materials, before querying the web portal to search for a particular metabolite. Additionally, the portal does not include datasets focused on

developmental biology, and raw LC–MS data files are not available for reprocessing.

To address this gap, we aimed to create an open-access dataset covering the circadian metabolome of multiple rat matrices (plasma, tissues, feces), ensuring the data are easily accessible and readily usable by the scientific community. We employed a combined extraction method for polar metabolites and complex lipids, followed by a multiplatform LC–MS-based approach, expanding the breadth and scope of covered metabolites. This enables a more thorough examination of circadian metabolic dynamics across different developmental stages and tissue types.

By sharing raw LC–MS instrumental files, we enable retrospective data mining, allowing for additional annotation of unknowns through MS/MS library searches and the potential discovery of novel metabolites. This study acquired LC–MS data in data-dependent acquisition (DDA) mode for all samples. We also employed iterative exclusion to remove background and previously selected high-abundance precursor ions, thereby increasing the likelihood of capturing MS/MS spectra from less abundant precursors. Additionally, LC–HDX-MS supported structural elucidation by reducing false positives using the number of exchangeable hydrogens to refine molecular formulas and distinguish isobaric species [87].

Adherence to the FAIR guiding principles ensures that metabolomics data generated during our analyses are Findable, Accessible, Interoperable, and Reusable (FAIR) [88]. This involves making raw instrumental LC–MS files publicly available, including samples, blanks, and quality control samples. Sharing data in a repository ensures accessibility to the scientific community. The FAIR principles also emphasize the importance of using harmonized formats to make data interoperable and ensure that data remains reusable with long-term validity, independent of time. By following these principles, we contribute to the reproducibility and transparency of metabolomics research.

Limitations of the study

This study used Wistar: Han rats, which may limit the generalizability of the findings to other species, including humans. Comparative analyses with genetically modified models could offer deeper insight into the role of specific genetic factors in shaping circadian metabolic rhythms. In addition, the utility of circadian metabolite atlases could be further enhanced by integrating non-sacrificial longitudinal sampling of biofluids (e.g., urine, blood) and feces under varied light and feeding conditions. Such an approach would allow for intra-individual tracking of metabolic rhythms, reduce inter-animal variability, and provide a more ecologically valid and clinically relevant picture of circadian metabolite dynamics.

From a technical perspective, LC–MS-based metabolomics is limited by metabolite coverage, ionization efficiency, and semi-quantitative reproducibility across diverse sample types [87]. Our combined extraction and LC–MS platforms [47] were optimized for high- and medium-abundance metabolites but may underrepresent low-abundance species. Detecting these would require specialized extraction protocols or alternative platforms with higher sensitivity. Although MS/MS data were acquired for all study samples, many metabolites remain unannotated due to limitations in current metabolomics databases. Expanding spectral libraries and incorporating advanced structural elucidation techniques could improve annotation rates [89].

Supplementary Information The online version contains supplementary material available at https://doi.org/10.1007/s00018-025-05783-w.

Acknowledgements The data were acquired at the Metabolomics Core Facility (https://metabolomics.fgu.cas.cz/) at the Institute of Physiology of the Czech Academy of Sciences.

Author contributions Conceptualization, T.C. and A.S.; methodology, L.R.K., P.H., M.N., J.H., M.P., O.K., M.S., O.F., A.S., and T.C.; investigation, L.R.K., P.H., M.N., J.H., M.P., O.K., M.S., O.F., A.S., and T.C.; writing—original draft, T.C. and A.S.; writing—review & editing, T.C., O.K., O.F., M.S., and A.S.; funding acquisition, T.C. and A.S.; resources, T.C. and A.S.; supervision, T.C. and A.S.

Funding Open access publishing supported by the institutions participating in the CzechELib Transformative Agreement. This work was supported by the Czech Science Foundation (20–21114S), Ministry of Education, Youth and Sport of the Czech Republic (LTAUSA19124), and the project National Institute for Research of Metabolic and Cardiovascular Diseases (Programme EXCELES, ID Project No. LX22NPO5104) funded by the European Union − Next Generation EU.

Data availability The Circadian Ontogenetic Metabolomics Atlas (COMA) is accessible at https://coma.metabolomics.fgu.cas.cz, and includes processed data used for circadian analysis across various developmental stages.
Raw files in mzXML format for all LC–MS platforms are available at https://doi.org/10.5281/zenodo.13843399 and also include metadata for study samples, method blanks, QC, and serial dilution samples for each LC–MS platform.

Declarations

Ethics approval All experiments were approved by the Animal Care and Use Committee of the Institute of Physiology (33/2019) and were conducted per the Animal Protection Law of the Czech Republic and the European Community Council directives 86/609/EEC. All possible efforts were made to minimize the suffering of the animals.

Competing interests The authors have no relevant financial or non-financial interests to disclose.

References

1. Bhadra U, Thakkar N, Das P, Bhadra MP (2017) Evolution of circadian rhythms: from bacteria to human. Sleep Med 35:49–61. https://doi.org/10.1016/j.sleep.2017.04.008
2. Panda S, Hogenesch JB, Kay SA (2002) Circadian rhythms from flies to human. Nature 417:329–335. https://doi.org/10.1038/417329a
3. Pittendrigh CS, Daan S (1976) A functional analysis of circadian pacemakers in nocturnal rodents. J Comp Physiol 106:223–252. https://doi.org/10.1007/Bf01417856
4. Hastings MH, Maywood ES, Brancaccio M (2018) Generation of circadian rhythms in the Suprachiasmatic nucleus. Nat Rev Neurosci 19:453–469. https://doi.org/10.1038/s41583-018-0026-z
5. Patke A, Young MW, Axelrod S (2020) Molecular mechanisms and physiological importance of circadian rhythms. Nat Rev Mol Cell Biol 21:67–84. https://doi.org/10.1038/s41580-019-0179-2
6. Ralph MR, Foster RG, Davis FC, Menaker M (1990) Transplanted Suprachiasmatic nucleus determines circadian period. Science 247:975–978. https://doi.org/10.1126/science.2305266
7. Reppert SM, Schwartz WJ (1983) Maternal coordination of the fetal biological clock in utero. Science 220:969–971. https://doi.org/10.1126/science.6844923
8. Moore RY (1991) Development of the Suprachiasmatic nucleus. In: Klein DC, Moore RY, Reppert SM (eds) Suprachiasmatic nucleus: the mind's clock. Oxford University Press, New York, pp 197–216
9. Bedont JL, Blackshaw S (2015) Constructing the suprachiasmatic nucleus: a watchmaker's perspective on the central clockworks. Front Syst Neurosci 9. https://doi.org/10.3389/Fnsys.2015.00074
10. Landgraf D, Koch CE, Oster H (2014) Embryonic development of circadian clocks in the mammalian Suprachiasmatic nuclei. Front Neuroanat 8. https://doi.org/10.3389/Fnana.2014.00143
11. Sumova A, Sladek M, Polidarova L, Novakova M, Houdek P (2012) Circadian system from conception till adulthood. Prog Brain Res 199:83–103. https://doi.org/10.1016/B978-0-444-59427-3.00005-8
12. Comas M, De Pietri Tonelli D, Berdondini L, Astiz M (2024) Ontogeny of the circadian system: a multiscale process throughout development. Trends Neurosci 47:36–46. https://doi.org/10.1016/j.tins.2023.11.004
13. Carmona-Alcocer V, Abel JH, Sun TC, Petzold LR, Doyle FJ 3rd, Simms CL et al (2018) Ontogeny of circadian rhythms and synchrony in the Suprachiasmatic nucleus. J Neurosci 38:1326–1334. https://doi.org/10.1523/JNEUROSCI.2006-17.2017
14. Shibata S, Moore RY (1987) Development of neuronal activity in the rat Suprachiasmatic nucleus. Brain Res 431:311–315. https://doi.org/10.1016/0165-3806(87)90220-3
15. Landgraf D, Achten C, Dallmann F, Oster H (2014) Embryonic development and maternal regulation of murine circadian clock function. Chronobiol Int 1–12. https://doi.org/10.3109/07420528.2014.986576
16. Sukumaran S, Almon RR, DuBois DC, Jusko WJ (2010) Circadian rhythms in gene expression: relationship to physiology, disease, drug disposition and drug action. Adv Drug Deliver Rev 62:904–917. https://doi.org/10.1016/j.addr.2010.05.009
17. Sakamoto K, Oishi K, Nagase T, Miyazaki K, Ishida N (2002) Circadian expression of clock genes during ontogeny in the rat heart. NeuroReport 13:1239–1242. https://doi.org/10.1097/00001756-200207190-00003
18. Sladek M, Jindrakova Z, Bendova Z, Sumova A (2007) Postnatal ontogenesis of the circadian clock within the rat liver. Am J Physiol-Reg I 292:R1224–R1229. https://doi.org/10.1152/ajpregu.00184.2006
19. Brown SA (2016) Circadian metabolism: from mechanisms to metabolomics and aedicine. Trends Endocrin Met 27:415–426. https://doi.org/10.1016/j.tem.2016.03.015
20. Gooley JJ, Chua ECP (2014) Diurnal regulation of lipid metabolism and applications of circadian lipidomics. J Genet Genomics 41:231–250. https://doi.org/10.1016/j.jgg.2014.04.001
21. Ch R, Chevallier O, Elliott CT (2020) Metabolomics reveal circadian control of cellular metabolism. TrAC-Trend Anal Chem 130:115986. https://doi.org/10.1016/J.Trac.2020.115986
22. Shen BY, Ma CX, Wu GL, Liu HB, Chen LH, Yang GR (2023) Effects of exercise on circadian rhythms in humans. Front Pharmacol 14:1282357. https://doi.org/10.3389/Fphar.2023.1282357
23. Davies SK, Ang JE, Revell VL, Holmes B, Mann A, Robertson FP et al (2014) Effect of sleep deprivation on the human metabolome. P Natl Acad Sci USA 111:10761–10766. https://doi.org/10.1073/pnas.1402663111
24. Kasukawa T, Sugimoto M, Hida A, Minami Y, Mori M, Honma S et al (2012) Human blood metabolite timetable indicates internal body time. P Natl Acad Sci USA 109:15036–15041. https://doi.org/10.1073/pnas.1207768109
25. Jeppe K, Ftouni S, Nijagal B, Grant LK, Lockley SW, Rajaratnam SMW et al (2024) Accurate detection of acute sleep deprivation using a metabolomic biomarker-A machine learning approach. Sci Adv 10:eadj6834. https://doi.org/10.1126/sciadv.adj6834
26. Minami Y, Kasukawa T, Kakazu Y, Iigo M, Sugimoto M, Ikeda S et al (2009) Measurement of internal body time by blood metabolomics. P Natl Acad Sci USA 106:9890–9895. https://doi.org/10.1073/pnas.0900617106
27. Li Q, Wang B, Qiu HY, Yan XJ, Cheng L, Wang QQ et al (2021) Chronic jet lag exacerbates lejunal and colonic microenvironment in mice. Front Cell Infect Mi 11:648175. https://doi.org/10.3389/Fcimb.2021.648175
28. Sato S, Dyar KA, Treebak JT, Jepsen SL, Ehrlich AM, Ashcroft SP et al (2022) Atlas of exercise metabolism reveals time-dependent signatures of metabolic homeostasis. Cell Metab 34:329–345. https://doi.org/10.1016/j.cmet.2021.12.016
29. Savikj M, Stocks B, Sato S, Caidahl K, Krook A, Deshmukh AS et al (2022) Exercise timing influences multi-tissue metabolome and skeletal muscle proteome profiles in type 2 diabetic patients - A randomized crossover trial. Metabolism 135:155268. https://doi.org/10.1016/j.metabol.2022.155268
30. Krishnaiah SY, Wu G, Altman BJ, Growe J, Rhoades SD, Coldren F et al (2017) Clock regulation of metabolites reveals coupling between transcription and metabolism. Cell Metab 25:961–974. https://doi.org/10.1016/j.cmet.2017.03.019
31. Loizides-Mangold U, Perrin L, Vandereycken B, Betts JA, Walhin JP, Templeman I et al (2017) Lipidomics reveals diurnal lipid oscillations in human skeletal muscle persisting in cellular myotubes cultured in vitro. P Natl Acad Sci USA 114:E8565–E8574. https://doi.org/10.1073/pnas.1705821114
32. Buijink MR, van Weeghel M, Gulersonmez MC, Harms AC, Rohling JHT, Meijer JH et al (2018) The influence of neuronal electrical activity on the mammalian central clock metabolome.

Metabolomics 14:122. https://doi.org/10.1007/S11306-018-1423-Z
33. Rahman SA, Gathungu RM, Marur VR, Hilaire MSA, Scheuermaier K, Belenky M et al (2023) Age-related changes in circadian regulation of the human plasma lipidome. Commun Biol 6:756. https://doi.org/10.1038/s42003-023-05102-8
34. Held NM, Buijink MR, Elfrink HL, Kooijman S, Janssens GE, Luyf ACM et al (2021) Aging selectively dampens Oscillation of lipid abundance in white and brown adipose tissue. Sci Rep 11:5932. https://doi.org/10.1038/S41598-021-85455-4
35. Liu XY, Tian XY, Shi QH, Sun HD, Li J, Tang XY et al (2022) Characterization of LC-MS based urine metabolomics in healthy children and adults. Peerj 10:e13545. https://doi.org/10.7717/peerj.13545
36. Lu XY, Solmonson A, Lodi A, Nowinski SM, Sentandreu E, Riley CL et al (2017) The early metabolomic response of adipose tissue during acute cold exposure in mice. Sci Rep 7. https://doi.org/10.1038/S41598-017-03108-X
37. Zhang ZD, Cheng L, Ma JX, Wang XM, Zhao YY (2022) Chronic cold exposure leads to daytime preference in the circadian expression of hepatic metabolic genes. Front Physiol 13:865627. https://doi.org/10.3389/Fphys.2022.865627
38. Dyar KA, Lutter D, Artati A, Ceglia NJ, Liu Y, Armenta D et al (2018) Atlas of circadian metabolism reveals system-wide coordination and communication between clocks. Cell 174:1571–1585. https://doi.org/10.1016/j.cell.2018.08.042
39. Tognini P, Samad M, Kinouchi K, Liu Y, Helbling JC, Moisan MP et al (2020) Reshaping circadian metabolism in the Suprachiasmatic nucleus and prefrontal cortex by nutritional challenge. P Natl Acad Sci USA 117:29904–29913. https://doi.org/10.1073/pnas.2016589117
40. Sprenger RR, Hermansson M, Neess D, Becciolini LS, Sorensen SB, Fagerberg R et al (2021) Lipid molecular timeline profiling reveals diurnal crosstalk between the liver and circulation. Cell Rep 34:108710. https://doi.org/10.1016/J.Celrep.2021.108710
41. Abbondante S, Eckel-Mahan KL, Ceglia NJ, Baldi P, Sassone-Corsi P (2016) Comparative circadian metabolomics reveal differential effects of nutritional challenge in the serum and liver. J Biol Chem 291:2812–2828. https://doi.org/10.1074/jbc.M115.681130
42. Sugimoto M, Ikeda S, Niigata K, Tomita M, Sato H, Soga T (2012) MMMDB: mouse multiple tissue metabolome database. Nucleic Acids Res 40:D809–D814. https://doi.org/10.1093/nar/gkr1170
43. Jain M, Ngoy S, Sheth SA, Swanson RA, Rhee EP, Liao R et al (2014) A systematic survey of lipids across mouse tissues. Am J Physiol-Endoc M 306:E854–E868. https://doi.org/10.1152/ajpendo.00371.2013
44. Rakusanova S, Fiehn O, Cajka T (2023) Toward Building mass spectrometry-based metabolomics and lipidomics atlases for biological and clinical research. TrAC-Trend Anal Chem 158:116825. https://doi.org/10.1016/j.trac.2022.116825
45. Houdek P, Sumova A (2014) In vivo initiation of clock gene expression rhythmicity in fetal rat Suprachiasmatic nuclei. PLoS ONE 9:e107360. https://doi.org/10.1371/journal.pone.0107360
46. Hricko J, Kulhava LR, Paucova M, Novakova M, Kuda O, Fiehn O et al (2023) Short-term stability of serum and liver extracts for untargeted metabolomics and lipidomics. Antioxidants 12:986. https://doi.org/10.3390/Antiox12050986
47. Cajka T, Hricko J, Rudl Kulhava L, Paucova M, Novakova M, Kuda O (2023) Optimization of mobile phase modifiers for fast LC-MS-based untargeted metabolomics and lipidomics. Int J Mol Sci 24:1987. https://doi.org/10.3390/ijms24031987
48. Shrestha TC, Suchmanova K, Houdek P, Sumova A, Ralph MR (2018) Implicit time-place conditioning alters Per2 mRNA expression selectively in striatum without shifting its circadian clocks. Sci Rep 8:15547. https://doi.org/10.1038/S41598-018-33637-Y
49. Greiner P, Houdek P, Sládek M, Sumová A (2022) Early rhythmicity in the fetal Suprachiasmatic nuclei in response to maternal signals detected by omics approach. Plos Biol 20:e3001637. https://doi.org/10.1371/journal.pbio.3001637
50. Sládek M, Houdek P, Sumová A (2019) Circadian profiling reveals distinct regulation of endocannabinoid system in the rat plasma, liver and adrenal glands by light-dark and feeding cycles. BBA-Mol Cell Biol L 1864:158533. https://doi.org/10.1016/J.Bbalip.2019.158533
51. Hughes ME, Hogenesch JB, Kornacker K (2010) JTK_CYCLE: an efficient nonparametric algorithm for detecting rhythmic components in genome-scale data sets. J Biol Rhythm 25:372–380. https://doi.org/10.1177/0748730410379711
52. Weger BD, Gobet C, David FPA, Atger F, Martin E, Phillips NE et al (2021) Systematic analysis of differential rhythmic liver gene expression mediated by the circadian clock and feeding rhythms. P Natl Acad Sci USA 118:e2015803118. https://doi.org/10.1073/pnas.2015803118
53. Tsugawa H, Ikeda K, Takahashi M, Satoh A, Mori Y, Uchino H et al (2020) A lipidome atlas in MS-DIAL 4. Nat Biotechnol 38:1159–1163. https://doi.org/10.1038/s41587-020-0531-2
54. Pang ZQ, Chong J, Zhou GY, Morais DAD, Chang L, Barrette M et al (2021) MetaboAnalyst 5.0: narrowing the gap between Raw spectra and functional insights. Nucleic Acids Res 49:W388–W396. https://doi.org/10.1093/nar/gkab382
55. Schwämmle V, Jensen ON (2018) VSClust: feature-based variance-sensitive clustering of omics data. Bioinformatics 34:2965–2972. https://doi.org/10.1093/bioinformatics/bty224
56. Hickey DS, Kirkland JL, Lucas SB, Lye M (1984) Analysis of Circadian-Rhythms by fitting a Least-Squares sine curve. Comput Biol Med 14:217–223. https://doi.org/10.1016/0010-4825(84)90008-8
57. Vondrackova M, Kopczynski D, Hoffmann N, Kuda O (2023) LORA, lipid Over-Representation analysis based on structural information. Anal Chem 95:12600–12604. https://doi.org/10.1021/acs.analchem.3c02039
58. Kováciková Z, Sládek M, Bendová Z, Illnerová H, Sumová A (2006) Expression of clock and clock-driven genes in the rat Suprachiasmatic nucleus during late fetal and early postnatal development. J Biol Rhythm 21:140–148. https://doi.org/10.1177/0748730405285876
59. Sládek M, Sumová A, Kováciková Z, Bendová Z, Laurinová K, Illnerová H (2004) Insight into molecular core clock mechanism of embryonic and early postnatal rat Suprachiasmatic nucleus. P Natl Acad Sci USA 101:6231–6236. https://doi.org/10.1073/pnas.0401149101
60. de Jonge NF, Mildau K, Meijer D, Louwen JJR, Bueschl C, Huber F et al (2022) Good practices and recommendations for using and benchmarking computational metabolomics metabolite annotation tools. Metabolomics 18:103. https://doi.org/10.1007/s11306-022-01963-y
61. Tsugawa H, Kind T, Nakabayashi R, Yukihira D, Tanaka W, Cajka T et al (2016) Hydrogen rearrangement rules: computational MS/MS fragmentation and structure Elucidation using MS-FINDER software. Anal Chem 88:7946–7958. https://doi.org/10.1021/acs.analchem.6b00770
62. Cajka T, Hricko J, Rakusanova S, Brejchova K, Novakova M, Rudl Kulhava L et al (2024) Hydrophilic interaction liquid chromatography–hydrogen/deuterium exchange–mass spectrometry (HILIC-HDX-MS) for untargeted metabolomics. Int J Mol Sci 25:2899. https://doi.org/10.3390/ijms25052899
63. Ferrell JM, Chiang JYL (2015) Circadian rhythms in liver metabolism and disease. Acta Pharm Sin B 5:113–122. https://doi.org/10.1016/j.apsb.2015.01.003

64. Segers A, Depoortere I (2021) Circadian clocks in the digestive system. Nat Rev Gastro Hepat 18:239–251. https://doi.org/10.1038/s41575-020-00401-5
65. Richards J, Gumz ML (2012) Advances in Understanding the peripheral circadian clocks. Faseb J 26:3602–3613. https://doi.org/10.1096/fj.12-203554
66. Takahashi JS (2017) Transcriptional architecture of the mammalian circadian clock. Nat Rev Genet 18:164–179. https://doi.org/10.1038/nrg.2016.150
67. Panda S (2016) Circadian physiology of metabolism. 354:1008–1015. https://doi.org/10.1126/science.aah4967
68. Firsov D, Bonny O (2018) Circadian rhythms and the kidney. Nat Rev Nephrol 14:626–635. https://doi.org/10.1038/s41581-018-0048-9
69. Chen LH, Yang GR (2015) Recent advances in circadian rhythms in cardiovascular system. Front Pharmacol 6:71. https://doi.org/10.3389/Fphar.2015.00071
70. Scheving LA (2000) Biological clocks and the digestive system. Gastroenterology 119:536–549. https://doi.org/10.1053/gast.2000.9305
71. Matsuo T, Yamaguchi S, Mitsui S, Emi A, Shimoda F, Okamura H (2003) Control mechanism of the circadian clock for timing of cell division in vivo. 302:255–259. https://doi.org/10.1126/science.1086271
72. Keller M, Mazuch J, Abraham U, Eom GD, Herzog ED, Volk HD et al (2009) A circadian clock in macrophages controls inflammatory immune responses. P Natl Acad Sci USA 106:21407–21412. https://doi.org/10.1073/pnas.0906361106
73. Sundar IK, Yao HW, Sellix MT, Rahman I (2015) Circadian molecular clock in lung pathophysiology. Am J Physiol-Lung C 309:L1056–L1075. https://doi.org/10.1152/ajplung.00152.2015
74. Chatterjee S, Ma K (2016) Circadian clock regulation of skeletal muscle growth and repair. F1000Res 5:1549. https://doi.org/10.12688/f1000research.9076.1
75. Froy O, Garaulet M (2018) The circadian clock in white and brown adipose tissue: mechanistic, endocrine, and alinical aspects. Endocr Rev 39:261–273. https://doi.org/10.1210/er.2017-00193
76. Olejnikova L, Polidarova L, Behuliak M, Sladek M, Sumova A (2018) Circadian alignment in a foster mother improves the offspring's pathological phenotype. J Physiol-London 596:5757–5775. https://doi.org/10.1113/JP275585
77. Koldovsky O, Hahn P, Hromadova M, Krecek J, Macho L (1995) Late effects of early nutritional manipulations. Physiol Res 44:357–360
78. Deota S, Pendergast JS, Kolthur-Seetharam U, Esser KA, Gachon F, Asher G et al (2025) The time is now: accounting for time-of-day effects to improve reproducibility and translation of metabolism research. Nat Metab 7:454–468. https://doi.org/10.1038/s42255-025-01237-6
79. Hatori M, Vollmers C, Zarrinpar A, DiTacchio L, Bushong EA, Gill S et al (2012) Time-restricted feeding without reducing caloric intake prevents metabolic diseases in mice fed a high-fat diet. Cell Metab 15:848–860. https://doi.org/10.1016/j.cmet.2012.04.019
80. Hsu PY, Harmer SL (2014) Global profiling of the circadian transcriptome using microarrays. Methods Mol Biol 1158:45–56. https://doi.org/10.1007/978-1-4939-0700-7_3
81. Brejchova K, Paluchova V, Brezinova M, Cajka T, Balas L, Durand T et al (2022) Triacylglycerols containing branched palmitic acid ester of hydroxystearic acid (PAHSA) are present in the breast milk and hydrolyzed by carboxyl ester lipase. Food Chem 388:132983. https://doi.org/10.1016/j.foodchem.2022.132983
82. Marsac R, Pinson B, Saint-Marc C, Olmedo M, Artal-Sanz M, Daignan-Fornier B et al (2019) Purine homeostasis is necessary for developmental timing, germline maintenance and muscle integrity in Caenorhabditis elegans. Genetics 211:1297–1313. https://doi.org/10.1534/genetics.118.301062
83. Jackman N, Ishii A, Bansal R (2009) Oligodendrocyte development and Myelin biogenesis: parsing out the roles of glycosphingolipids. Physiology 24:290–297. https://doi.org/10.1152/physiol.00016.2009
84. Morris AI, Little JM, Lester R (1983) Development of the bile acid pool in rats from neonatal life through puberty to maturity. Digestion 28:216–224. https://doi.org/10.1159/000198991
85. Allen LH (2012) B vitamins in breast milk: relative importance of maternal status and intake, and effects on infant status and function. Adv Nutr 3:362–369. https://doi.org/10.3945/an.111.001172
86. Ceglia N, Liu Y, Chen SW, Agostinelli F, Eckel-Mahan K, Sassone-Corsi P et al (2018) CircadiOmics: circadian omic web portal. Nucleic Acids Res 46:W157–W162. https://doi.org/10.1093/nar/gky441
87. Rakusanova S, Cajka T (2024) Tips and tricks for LC-MS-based metabolomics and lipidomics analysis. TrAC-Trend Anal Chem 180:117940. https://doi.org/10.1016/J.Trac.2024.117940
88. Wilkinson MD, Dumontier M, Aalbersberg IJ, Appleton G, Axton M, Baak A et al (2016) Comment: the FAIR guiding principles for scientific data management and stewardship. Sci Data 3:160018. https://doi.org/10.1038/Sdata.2016.18
89. Kind T, Tsugawa H, Cajka T, Ma Y, Lai ZJ, Mehta SS et al (2018) Identification of small molecules using accurate mass MS/MS search. Mass Spectrom Rev 37:513–532. https://doi.org/10.1002/mas.21535

Authors and Affiliations

Lucie Rudl Kulhava[1] · Pavel Houdek[1] · Michaela Novakova[1] · Jiri Hricko[1] · Michaela Paucova[1] · Ondrej Kuda[1] · Martin Sladek[1] · Oliver Fiehn[2] · Alena Sumova[1] · Tomas Cajka[1]

✉ Alena Sumova
alena.sumova@fgu.cas.cz

✉ Tomas Cajka
tomas.cajka@fgu.cas.cz

[1] Institute of Physiology of the Czech Academy of Sciences, Videnska 1083, Prague 14200, Czech Republic

[2] University of California, Davis, 451 Health Sciences Drive, Davis, CA 95616, USA

Supplementary information

Circadian ontogenetic metabolomics atlas: an interactive resource with insights from rat plasma, tissues, and feces

Lucie Rudl Kulhava,[1,†] Pavel Houdek,[1,†] Michaela Novakova,[1,†] Jiri Hricko,[1] Michaela Paucova,[1] Ondrej Kuda,[1] Martin Sladek,[1] Oliver Fiehn,[2] Alena Sumova,[1,‡,*] Tomas Cajka[1,‡,*]

[1] Institute of Physiology of the Czech Academy of Sciences, Videnska 1083, Prague, 14200, Czech Republic

[2] University of California, Davis, 451 Health Sciences Drive, Davis, CA, 95616, United States

[†] These authors contributed equally

[‡] Senior authors

[*] E-mails: Alena Sumova; alena.sumova@fgu.cas.cz and Tomas Cajka; tomas.cajka@fgu.cas.cz

DOI: 10.1007/s00018-025-05783-w

Supplementary materials and methods

Figures S1–S8

Supplementary materials and methods

Reagents for LC–MS-based metabolomics

For sample extraction, methanol (J.T.Baker, catalog no. 9822), methyl *tert*-butyl ether (Honeywell, catalog no. 34875), and water (VWR, catalog no. 83645.320) were used. LC–MS-grade solvents for mobile phases included acetonitrile (Honeywell, catalog no. 34967), methanol (J.T.Baker, catalog no. 9822), water (VWR, catalog no. 83645.320), and isopropanol (Supelco, catalog no. 1027812500) [1]. Mobile phase modifiers, such as ammonium formate (Supelco, catalog no. 70221), ammonium acetate (Sigma–Aldrich, catalog no. A7330), formic acid (VWR, catalog no. 84865.260), and acetic acid (VWR, catalog no. 84874.180), were also of LC–MS-grade quality [1]. For HILIC–HDX-MS experiments, ammonium formate-d_5 (Merck, catalog no. 795119), formic acid-d_2 (CDN Isotopes, catalog no. DLM-286-PK), deuterium oxide (Merck, catalog no. 617385), and N^1-acetylspermidine (Cayman Chemical, catalog no. 9001535) were used [2]. Internal standards were obtained from Avanti, Cayman Chemical, CDN Isotopes, Merck, Sigma–Aldrich, and Supelco.

Sample extraction

For the sample extraction, a biphasic solvent system of methanol, methyl *tert*-butyl ether (MTBE), and water was used to isolate complex lipids, polar metabolites, and exposome compounds (LIMeX workflow) [1, 3-5]. An aliquot of 25 µL was used for plasma, and approximately 20 mg was used for tissues, with exceptions for mPFC (E19: 2–10 mg; P2–P28: 10 mg), feces (E19: 1.8–5.2 mg; P2–P28: 10 mg), and SCN (dissected SCN was isolated by a pre-cooled microbiopsy punch, resulting in a cylindrical sample of SCN-containing frozen tissue with a 0.3 mm diameter and approximately 0.4 mm height).

Plasma. A volume of 165 µL methanol containing internal standards (CAR 14:0-d_9, CAR 16:0-d_3, CAR 18:0-d_3, Cer d18:1/17:0, cholesterol-d_7, CL 16:0/16:0/16:0/16:0, DG 12:0/12:0/0:0, DG 18:1/0:0/18:1-d_5, DG 18:1/2:0/0:0, Hex-Cer d18:1/17:0, LPC 17:1, LPE 17:1, LPG 17:1, LPS 17:1, MG 17:0/0:0/0:0, oleic acid-d_9, PC 15:0/18:1-d_7, PE 17:0/17:0, PG 17:0/17:0, PI 15:0/18:1-d_7, PS 17:0/17:0, SM d18:1/17:0, sphingosine d17:1, TG 17:0/17:1/17:0-d_5, TG 20:0/20:1/20:0-d_5) was added to plasma aliquot and shaken (30 s) followed by addition of 600 µL of MTBE with internal standard (CE 22:1) and shaking (30 s). Then, 165 µL of 10% methanol containing also internal standards (3-hydroxybutyric acid-d_4, acetylcholine-d_4, alanine($^{13}C_3$; ^{15}N), arginine($^{13}C_6$; $^{15}N_4$), aspartic acid($^{13}C_4$; ^{15}N), betaine-d_9, butyrobetaine-d_9, caffeine-d_9, carnitine-d_9, CAR 2:0-d_3, CAR 3:0-d_3, CAR 4:0-d_3, CAR 6:0-d_3, CAR 8:0-d_3, CAR 10:0-d_3, CAR 12:0-d_9, choline-d_9, citrulline-d_4, cotinine-d_3, creatine-d_3, creatinine-d_3, cystine($^{13}C_6$; $^{15}N_2$), glucose-d_7, glutamic acid($^{13}C_5$; ^{15}N), glycine($^{13}C_2$; ^{15}N), histidine($^{13}C_6$; $^{15}N_3$), isoleucine($^{13}C_6$; ^{15}N), leucine($^{13}C_6$; ^{15}N), lysine($^{13}C_6$; $^{15}N_2$), metformin-d_6, methionine($^{13}C_5$; ^{15}N), *N*-methylnicotinamide-d_4, ornithine-d_6, phenylalanine($^{13}C_9$; ^{15}N), proline($^{13}C_5$; ^{15}N), serine($^{13}C_3$; ^{15}N), succinic acid-d_4, threonine($^{13}C_4$; ^{15}N), trimethylamine *N*-oxide-d_9, tyrosine($^{13}C_9$; ^{15}N), valine($^{13}C_5$; ^{15}N)) was added, the tubes were vortexed (10 s) and centrifuged (16,000 rpm, 5 min, 4 °C).

The first aliquot of 60 µL of the bottom phase was collected and evaporated to analyze polar metabolites. The dry plasma extracts were resuspended in 60 µL of an acetonitrile/water (4:1) mixture with two internal standards (12-[[(cyclohexylamino)carbonyl]amino]-dodecanoic acid (CUDA) and Val-Tyr-Val), shaken (30 s), centrifuged (16,000 rpm, 5 min, 4 °C), and analyzed using the HILIC metabolomics platforms in positive and negative electrospray ionization (ESI) mode. The second 60 µL aliquot of the bottom phase was mixed with 180 µL of an isopropanol/acetonitrile (1:1) mixture, shaken (30 s), centrifuged (16,000 rpm, 5 min, 4 °C), and the supernatant was evaporated. The dry plasma extracts were resuspended in 5% methanol/0.2% formic acid containing two internal standards (CUDA and Val-Tyr-Val), shaken (30 s), centrifuged (16,000 rpm, 5 min, 4 °C), and analyzed using the RPLC metabolomics platform in positive and negative ESI mode. An aliquot of 100 µL of the upper phase was collected and evaporated to analyze complex lipids. The dry extracts were resuspended in 100 µL methanol containing internal standards (arachidonic acid-d_{11}, CAR 24:0-d_4, CE 18:1-d_7, Cer d18:1/10:0, CUDA, DG 15:0/18:1-d_7, GlcCer d18:1/12:0, LPC 18:1-d_7, LPE 18:1-d_7, LPG 13:0, LPI 17:1, LPS 13:0, MG 18:1-d_7, PC 13:0/13:0, PE 15:0/18:1-d_7, PG 15:0/18:1-d_7, PI 8:0/8:0, PS 14:0/14:0, sGalCer d18:1/12:0, SM d18:1/12:0, sphingosine 18:1-d_7, TG 15:0/18:1/15:0-d_7), shaken (30 s), centrifuged (16,000 rpm, 5 min, 4 °C), and analyzed using the RPLC lipidomics platform in positive and negative ESI mode.

Tissues and feces. Tissue and feces sample aliquots were homogenized with 275 µL methanol containing internal standards using a grinder (frequency 1/s: 30, 1.5 min). Then, 1 mL of MTBE with internal standard was added, and the tubes were shaken (30 s). A volume of 275 µL 10% methanol was added, and after vortexing (10 s), the tubes were centrifuged (16,000 rpm, 5 min, 4 °C). Analysis of polar metabolites was performed similarly to that of plasma samples. For complex lipid analysis, 100 µL aliquots were collected for feces and tissues except for mPFC and SCN; in this case, 400 µL aliquots were taken to increase the lipidome coverage. After solvent evaporation, the dry extracts were resuspended in 100 µL (feces), 300 µL (non-fat tissues), or 50 µL (mPFC, SCN) methanol containing a mixture of internal standards, shaken (30 s), centrifuged (16,000 rpm, 5 min, 4 °C), and analyzed using the RPLC lipidomics platform in positive and negative ESI mode.

Adipose tissues. Adipose tissue sample aliquots were homogenized with 275 µL methanol containing internal standards using a grinder (frequency 1/s: 30, 1.5 min). Then, 1 mL of MTBE with internal standard was added, and the tubes were shaken (30 s). A volume of 275 µL 10% methanol was added, and after vortexing (10 s), the tubes were centrifuged (16,000 rpm, 5 min, 4 °C). Analysis of polar metabolites was performed similarly to that of plasma samples. For analysis of minor complex lipids, 100 µL of the upper organic phase was collected, evaporated, resuspended using 100 µL 90% methanol with an internal standard (CUDA), shaken (30 s), centrifuged (16,000 rpm, 5 min, 4 °C), and analyzed using the RPLC lipidomics platform in positive and negative ESI mode. For analysis of abundant triacylglycerols, 10 µL aliquot of the upper organic phase was collected, evaporated, resuspended using 1 mL methanol containing a mixture of internal standards, shaken (30 s), centrifuged (16,000 rpm, 5 min, 4 °C), and analyzed using the RPLC lipidomics platform in positive ESI mode.

LC–MS analysis

For LC–MS analysis, a Vanquish UHPLC system (Thermo Fisher Scientific), a heated electrospray ionization (HESI-II) probe (Thermo Fisher Scientific), and a Q Exactive Plus mass spectrometer (Thermo Fisher Scientific) were used [4].

Polar metabolites. For the separation of polar metabolites based on the HILIC mechanism, the following conditions were used: an ACQUITY Premier BEH Amide column (50 mm length × 2.1 mm i.d.; 1.7 µm particle size) with a VanGuard FIT cartridge (5 mm length × 2.1 mm i.d.; 1.7 µm particle size) (Waters, catalog no. 186010380); column compartment temperature, 45 °C; column flow rate, 0.8 mL/min; mobile phase A, water with 10 mM ammonium formate and 0.125% formic acid; mobile phase B, acetonitrile/water (95:5) with 10 mM ammonium formate and 0.125% formic acid; gradient run, 0 min 100% B, 0–0.5 min 100% B, 0.5–2.0 min from 100% to 70% B, 2.0–2.6 min from 70% to 30% B, 2.6–3.2 min from 30% to 100% B, 3.2–3.4 min 100% B +1 min preinjection steps; injection volumes, 0.3–1 µL (based on the matrix) in ESI(+) and 5 µL in ESI(−) [4]. For the HILIC–HDX-MS platform, the conditions were identical, except for using mobile phase A consisting of D_2O with 10 mM ammonium formate-d_5 and 0.125% formic acid-d_2, and mobile phase B made from acetonitrile/D_2O (95:5) with 7.5 mM ammonium formate-d_5 and 0.125% formic acid-d_2 [2].

For the separation of polar metabolites based on the RPLC mechanism, the following conditions were applied: an ACQUITY Premier HSS T3 column (50 mm length × 2.1 mm i.d.; 1.8 µm particle size) with a VanGuard FIT cartridge (5 mm length × 2.1 mm i.d.; 1.8 µm particle size) (Waters, catalog no. 186009470); column compartment temperature, 45 °C; column flow rate, 0.6 mL/min; mobile phase A, water with 0.2% formic acid; mobile phase B, methanol with 0.1% formic acid; gradient run, 0 min 1% B, 0–0.5 min 1% B, 0.5–2 min from 1% to 60% B, 2–2.3 min from 60% to 99% B, 2.3–2.8 min 99% B, 2.8–2.9 min from 99% to 1% B, 2.9–3.4 min 1% B + 1 min preinjection steps; injection volumes, 1–2 µL (based on the matrix) in ESI(+) and 5 µL in ESI(−) [4].

The ion source parameters were as follows: sheath gas pressure, 60 arbitrary units (a.u.); aux gas flow, 25 a.u.; sweep gas flow, 4 a.u.; capillary temperature, 300 °C; aux gas heater temperature, 475 °C; spray voltage: 3.5 kV for ESI(+), −3.0 kV for ESI(−). The MS settings were: MS1 mass range, *m*/*z* 60–900; MS1 resolving power, 17,500 FWHM; AGC target, 1e6; maximum IT, 50 ms; spectrum data type, centroid; the number of data-dependent scans per cycle, 2; MS/MS resolving power, 17,500 FWHM; AGC target, 1e5; maximum IT, 50 ms; spectrum data type, centroid; isolation window, 1 *m*/*z*; minimum AGC target, 5e2; dynamic exclusion, 2 s; exclude isotopes, on; normalized collision energies: 20, 30, and 40% [4].

Complex lipids. For the separation of complex lipids based on the RPLC mechanism, the following conditions were used: an ACQUITY Premier BEH C18 column (50 mm length × 2.1 mm i.d.; 1.7 µm particle size) with a VanGuard

FIT cartridge (5 mm length × 2.1 mm i.d.; 1.7 µm particle size) (Waters, catalog no. 186009455); column compartment temperature, 65 °C; column flow rate, 0.8 mL/min. For ESI(+), the conditions were as follows: mobile phase A, 60:40 acetonitrile/water with 10 mM ammonium formate and 0.1% formic acid; mobile phase B, 90:10:0.1 isopropanol/acetonitrile/water with 10 mM ammonium formate and 0.1% formic acid; gradient run, 0 min 15% B, 0–0.5 min from 15% to 30% B, 0.5–0.6 min from 30% to 50% B, 0.6–2.8 min from 50% to 80% B, 2.8–3.2 min from 80% to 99% B, 3.2–3.4 min 99% B, 3.4–3.5 min from 99% to 15% B, 3.5–3.7 min 15% B + 1 min preinjection steps. For ESI(−), the conditions were as follows: mobile phase A, 60:40 acetonitrile/water with 10 mM ammonium acetate and 0.1% acetic acid; mobile phase B, 90:10:0.1 isopropanol/acetonitrile/water with 10 mM ammonium acetate and 0.1% acetic acid; gradient run, 0 min 15% B, 0–0.5 min from 15% to 30% B, 0.5–0.6 min from 30% to 50% B, 0.6–2.4 min from 50% to 75% B, 2.4–2.5 min from 75% to 99% B, 2.5–2.9 min 99% B, 2.9–3.0 min from 99% to 15% B, 3.0–3.2 min 15% B + 1 min preinjection steps; injection volumes, 0.3–5 µL (based on the matrix) in ESI(+) and 5 µL in ESI(−) [4].

The ion source parameters were as follows: sheath gas pressure, 60 a.u.; aux gas flow, 25 a.u.; sweep gas flow, 4 a.u.; capillary temperature, 300 °C; aux gas heater temperature, 475 °C; spray voltage: 3.5 kV for ESI(+), −3.0 kV for ESI(−). The MS settings were: MS1 mass range, *m*/*z* 200–1700 for ESI(+), *m*/*z* 199–1700 for ESI(−); MS1 resolving power, 35,000 FWHM; AGC target, 1e6; maximum IT, 100 ms; spectrum data type, centroid; the number of data-dependent scans per cycle, 2; MS/MS resolving power, 17,500 FWHM; AGC target, 1e5; maximum IT, 50 ms; spectrum data type, centroid; isolation window, 1 *m*/*z*; minimum AGC target, 5e2; dynamic exclusion, 2 s; exclude isotopes, on; normalized collision energies: 20% for ESI(+) and 10, 20, and 30% for ESI(−) [4].

Enhancing the acquisition of MS/MS spectra. During LC–MS analysis, we implemented critical rules to enhance metabolome coverage by increasing the acquired MS/MS spectra for metabolite annotation. These rules involved optimizing the number of MS/MS scans per cycle, establishing an appropriate threshold for precursor ion selection, using an exclusion list, employing filters for precursor selection (e.g., isotope exclusion function and charge state), and conducting data-dependent acquisition (DDA) on all measured samples for optimal performance [6]. For each LC–MS platform, an initial exclusion list, consisting of *m*/*z* values across the entire retention time range (i.e., background contamination, impurities from mobile phases), was generated following the injection of the resuspension solvent. Subsequently, MS1 acquisition and DDA-MS/MS were conducted for all pool QC and SQC samples. The ProteoWizard software was employed to generate an MS2 file with specific parameters (peak picking (vendor): level, 2-2; msLevel, 2-2; threshold, absolute 0.0001 most intense; output, MS2). This MS2 file was then processed by an R script (https://secim.ufl.edu/secim-tools/ie-omics) [7]. An updated exclusion list in CSV format was exported, containing both previously excluded *m*/*z* values (IE-1) and newly excluded *m*/*z* values (IE-2), primarily associated with high-abundance precursor ions of metabolites. MS/MS spectra were acquired for high-abundance precursor ions in 15 samples (method IE-1) within each group of samples during the run. Simultaneously, MS/MS spectra for low-abundance precursor ions were acquired for the remaining 20 samples within each group (method IE-2). Both methods (IE-1 and IE-2) alternated during the injection of SQC samples. Additional MS/MS spectra were also acquired using SQC samples and splitting the MS1 mass range into 10 sub-mass ranges to select precursor ions.

Quality control. Due to the high number of samples analyzed, we implemented various quality control measures throughout the metabolomics analyses to ensure data reliability (**Fig. S1**), specifically (i) randomization of the actual samples within the sequence based on the matrix and developmental stage, (ii) injection of quality control (QC) pool samples for each matrix at the beginning, the end, and between every 35 actual samples (for particular matrix), (iii) injection of superior QC samples (SQC), a mix of pool QC samples of all matrices, at the beginning and the end of the sequence and between every 35 actual samples throughout the whole sequence regardless the matrix, (iv) analysis of method blanks, (v) serial dilution of SQC sample (0, 1/16, 1/8, 1/4, 1/2, 1), and (vi) checking the peak shape and the intensity of spiked internal standards and the internal standards added prior to injection [4].

LC–MS data processing

All the LC–MS raw files were converted into ABF format using an ABF converter (https://www.reifycs.com/abfconverter). MS-DIAL v. 4.92 software was used to process converted LC–MS files, including peak detection, deconvolution, alignment, and metabolite annotation (https://systemsomicslab.github.io/compms/msdial/main.html) [8]. The following parameters were used: (i) data collection: MS1 tolerance, 0.01; MS2 tolerance, 0.025; (ii) peak detection: minimum peak height, 20,000; mass

slice width, 0.05; smoothing method, Linear Weighted Moving Average; smoothing level, 2; (iii) MS/MS identification setting: accurate mass tolerance (MS1), 0.01; accurate mass tolerance (MS2), 0.025; identification score cut off, 80%; (iv) alignment: retention time tolerance, 0.05 min; MS1 tolerance, 0.01 Da; peak count filter, 5%; gap filling by compulsion, true.

Metabolites were annotated based on retention time–accurate mass (MS1, MS/MS) match from an in-house spectral library (MSI Level 1) along with MS/MS libraries from various sources (NIST20, MassBank.us, and MS-DIAL MS/MS library v. 15) (MSI Level 2). Complex lipids were annotated using *in-silico* MS/MS spectra available in MS-DIAL software (MSI Levels 2–3). The exported sets were further filtered based on a max sample peak height/blank peak height average <10, an R^2 <0.8 from a dilution series of SQC samples, and a relative standard deviation (RSD) >30% from SQC samples [4]. Data were then normalized using locally estimated scatterplot smoothing (LOESS) with SQC samples injected between 35 actual study samples, and for tissues and feces, based on the amount taken for the analysis. Before statistical analysis, metabolites with more than 50% missing values for each developmental stage and matrix were excluded, and missing data were imputed by replacing 1/5 of the minimal positive values of their corresponding variables for each developmental stage and matrix.

MS-FINDER software v. 3.60 (https://systemsomicslab.github.io/compms/msfinder/main.html) [9] was used for the structure elucidation of N^1-acetylspermidine with the following parameters: mass tolerance (MS1), 0.005 Da; mass tolerance (MS2), 0.005; relative abundance cut-off, 0.1%; LEWIS and SENIOR check, checked; isotopic ratio tolerance, 20%; element ratio check, common range (99.7%); element selection, O, N, P, S; tree depth, 2; local databases + MiNEs + PubChem, checked [2].

ProteoWizard software v. 3.0.22342 (https://proteowizard.sourceforge.io) [10] was used to convert raw LC–MS instrumental files to mzXML format for all platforms.

References

1. Cajka T, Hricko J, Rudl Kulhava L, Paucova M, Novakova M and Kuda O (2023) Optimization of mobile phase modifiers for fast LC-MS-based untargeted metabolomics and lipidomics. Int J Mol Sci 24:1987. https://doi.org/10.3390/ijms24031987
2. Cajka T, Hricko J, Rakusanova S, Brejchova K, Novakova M, Rudl Kulhava L, et al. (2024) Hydrophilic interaction liquid chromatography–hydrogen/deuterium exchange–mass spectrometry (HILIC-HDX-MS) for untargeted metabolomics. Int J Mol Sci 25:2899. https://doi.org/10.3390/ijms25052899
3. Lopes M, Brejchova K, Riecan M, Novakova M, Rossmeisl M, Cajka T, et al. (2021) Metabolomics atlas of oral 13C-glucose tolerance test in mice. Cell Rep 37:109833. https://doi.org/10.1016/J.Celrep.2021.109833
4. Hricko J, Kulhava LR, Paucova M, Novakova M, Kuda O, Fiehn O, et al. (2023) Short-term stability of serum and liver extracts for untargeted metabolomics and lipidomics. Antioxidants 12:986. https://doi.org/10.3390/Antiox12050986
5. Janovska P, Melenovsky V, Svobodova M, Havlenova T, Kratochvilova H, Haluzik M, et al. (2020) Dysregulation of epicardial adipose tissue in cachexia due to heart failure: the role of natriuretic peptides and cardiolipin. J Cachexia Sarcopenia Muscle 11:1614-1627. https://doi.org/10.1002/jcsm.12631
6. Defossez E, Bourquin J, Reuss S, Rasmann S and Glauser G (2021) Eight key rules for successful data-dependent acquisition in mass spectrometry-based metabolomics. Mass Spectrom Rev 42:131-143. https://doi.org/10.1002/mas.21715
7. Koelmel JP, Kroeger NM, Gill EL, Ulmer CZ, Bowden JA, Patterson RE, et al. (2017) Expanding lipidome coverage using LC-MS/MS data-dependent acquisition with automated exclusion list generation. J Am Soc Mass Spectr 28:908-917. https://doi.org/10.1007/s13361-017-1608-0
8. Tsugawa H, Ikeda K, Takahashi M, Satoh A, Mori Y, Uchino H, et al. (2020) A lipidome atlas in MS-DIAL 4. Nat Biotechnol 38:1159-1163. https://doi.org/10.1038/s41587-020-0531-2
9. Tsugawa H, Kind T, Nakabayashi R, Yukihira D, Tanaka W, Cajka T, et al. (2016) Hydrogen rearrangement rules: Computational MS/MS fragmentation and structure elucidation using MS-FINDER software. Anal Chem 88:7946-7958. https://doi.org/10.1021/acs.analchem.6b00770
10. Chambers MC, Maclean B, Burke R, Amodei D, Ruderman DL, Neumann S, et al. (2012) A cross-platform toolkit for mass spectrometry and proteomics. Nat Biotechnol 30:918-920. https://doi.org/10.1038/nbt.2377

	Injection order →									
Solvent prerun	S	O	L	V	E	N	T	R	U	N
SST, preinjection SQC	SST	SQC								
SQC & dilution series of SQC	SQC	SD	SD	SD	SD	SD	SD			
SQC	SQC									
QC, matrix 1	QC									
Randomized samples, matrix 1, devel. stage 1	S	S	S	S	S	S	S	S	S	S
	S	S	S	S	S	S	S	S	S	S
	S	S	S	S	S	S	S	S	S	S
	S	S	S	S	S					
SQC	SQC									
QC, matrix 1	QC									
Randomized samples, matrix 1, devel. stage 2	S	S	S	S	S	S	S	S	S	S
	S	S	S	S	S	S	S	S	S	S
	S	S	S	S	S	S	S	S	S	S
	S	S	S	S	S					
SQC	SQC									
QC, matrix 1	QC									
Randomized samples, matrix 1, devel. stage 3	S	S	S	S	S	S	S	S	S	S
	S	S	S	S	S	S	S	S	S	S
	S	S	S	S	S	S	S	S	S	S
	S	S	S	S	S					
QC, matrix 1	QC									
SQC	SQC									
...	...									
SQC	SQC									
QC, matrix 10	QC									
Randomized samples, matrix 10, devel. stage 1	S	S	S	S	S	S	S	S	S	S
	S	S	S	S	S	S	S	S	S	S
	S	S	S	S	S	S	S	S	S	S
	S	S	S	S	S					
SQC	SQC									
QC, matrix 10	QC									
Randomized samples, matrix 10, devel. stage 2	S	S	S	S	S	S	S	S	S	S
	S	S	S	S	S	S	S	S	S	S
	S	S	S	S	S	S	S	S	S	S
	S	S	S	S	S					
QC, matrix 10	QC									
SQC	SQC									
...	...									
SQC	SQC									
Blanks	BL	BL	BL	BL	BL	BL	BL	BL	BL	BL
...	...									
SQC & dilution series of SQC	SQC	SD	SD	SD	SD	SD	SD			
SQC, MS/MS acquisition for MS1 sub-mass ranges	SQC	SQC	SQC	SQC	SQC	SQC	SQC	SQC	SQC	SQC

Fig. S1 Schematic overview of the LC–MS data acquisition sequence. The sequence begins with solvent injections to equilibrate the LC–MS platform, followed by a system suitability test (SST) using a mixture of standards, injections of superior quality control (SQC) samples, and a dilution series of the SQC. Each randomized sample set, organized by matrix and developmental stage, is bracketed by injections of matrix-specific QC samples and the SQC (a pooled sample of all matrix-based QCs). The sequence also includes method blank injections to monitor background contamination.

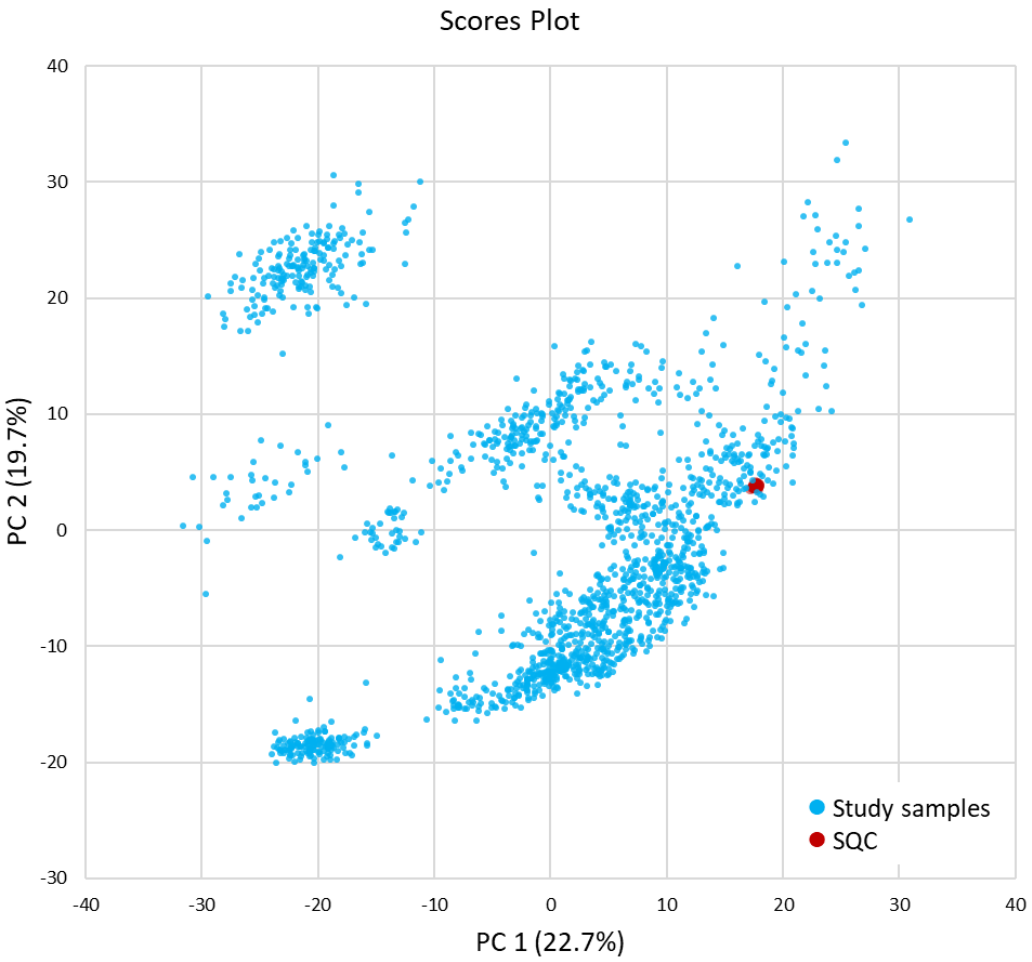

Fig. S2 PCA of 1610 study samples (blue) and corresponding SQC samples (red), based on 851 metabolites. The tight clustering of SQC samples indicates low technical variability and high reliability of the metabolomic analyses.

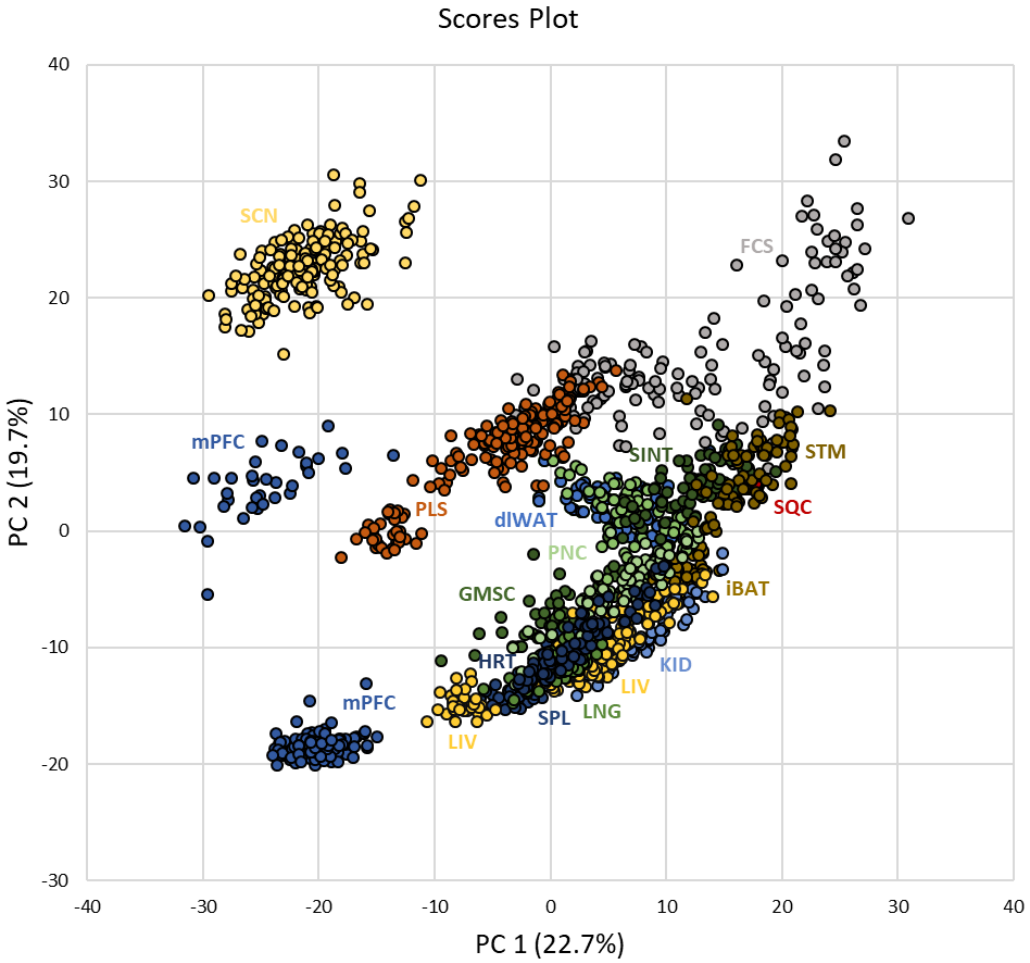

Fig. S3 PCA of study samples colored by a particular matrix and SQC samples based on 851 metabolites. Legend: dorso-lumbar white adipose tissue (dlWAT), feces (FCS), gastrocnemius skeletal muscle (GMSC), heart (HRT), intrascapular brown adipose tissue (iBAT), intrascapular white adipose tissue (isWAT), kidney (KID), liver (LIV), lungs (LNG), medial prefrontal cortex (mPFC), pancreas (PNC), plasma (PLS), small intestine (jejunum) (SINT), spleen (SPL), stomach (STM), suprachiasmatic nucleus (SCN).

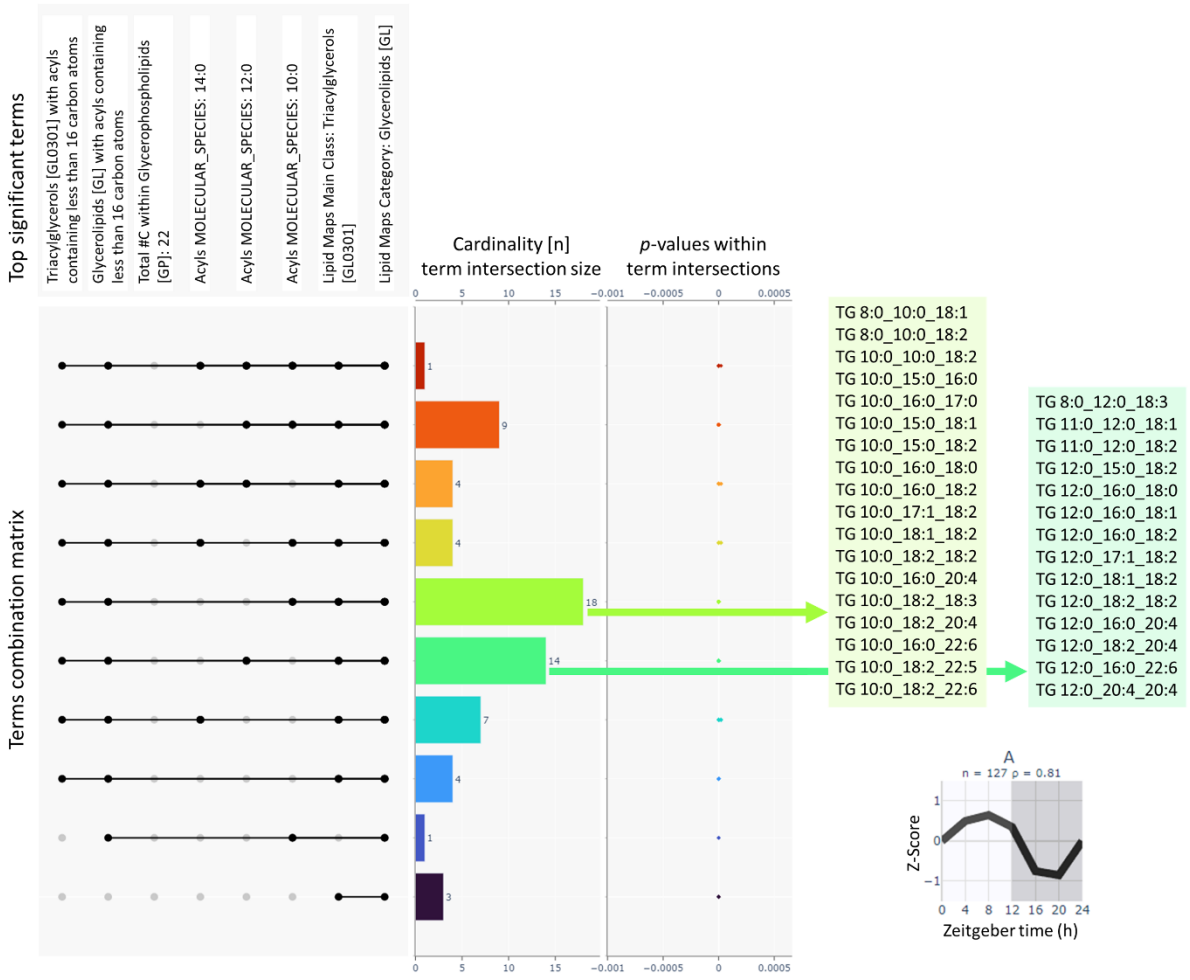

Fig. S4 Example of results from lipid over-representation analysis for plasma at P28, specifically focusing on cluster A. The UpSet plot displays the intersection of over-expressed terms, representing structural characteristics. Cardinality is then sorted based on the total number of term intersections, with each cluster containing lipids that share a particular structural feature. For enrichment analysis, the Fisher exact test (greater) followed by multiple hypothesis testing (FDR (Benjamini–Hochberg) and an alpha level of 0.005 was used.

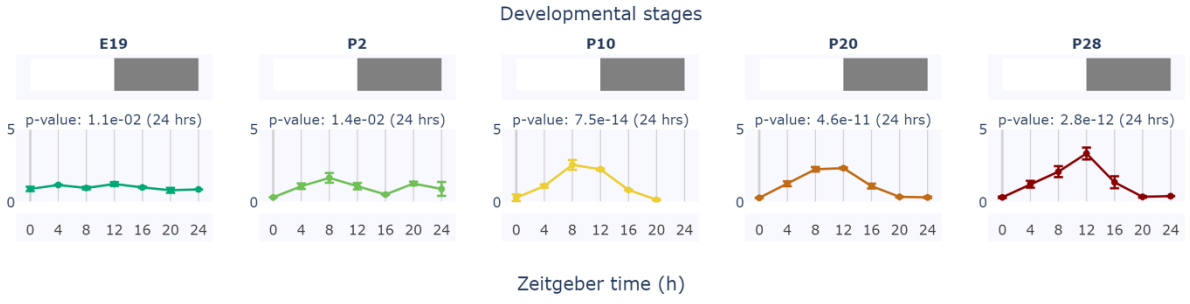

Fig. S5 Expression of clock gene *Per2* in the SCN at different developmental stages.

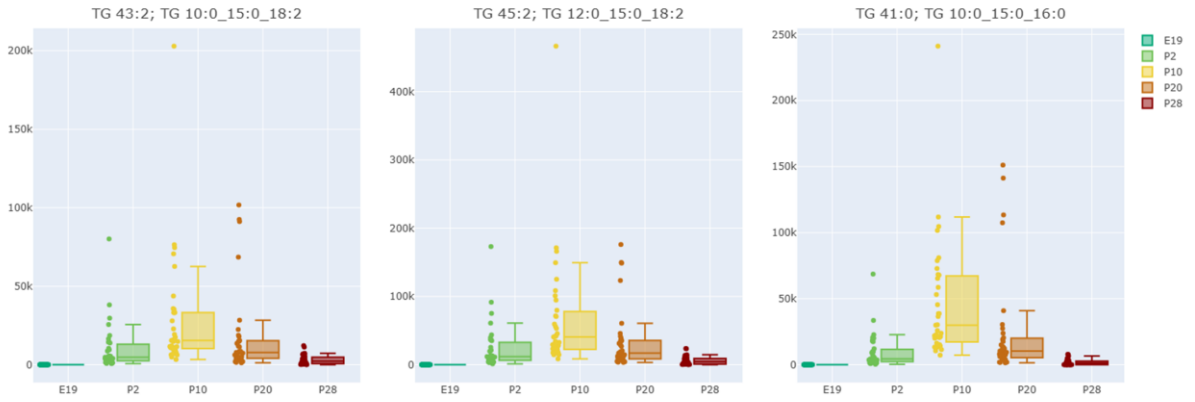

Fig. S6 Profiles of selected plasma triacylglycerols (TGs) containing short-chain saturated fatty acids. TGs were selected based on PLS-DA with a VIP score>1.

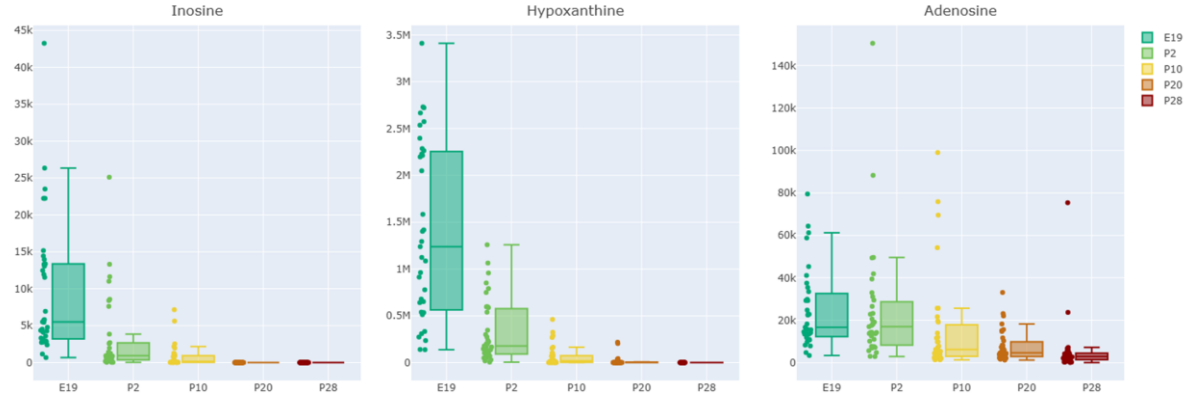

Fig. S7 Profiles of inosine, hypoxanthine, and adenosine detected in plasma based on developmental stage. Metabolites were selected based on PLS-DA with a VIP score>1.

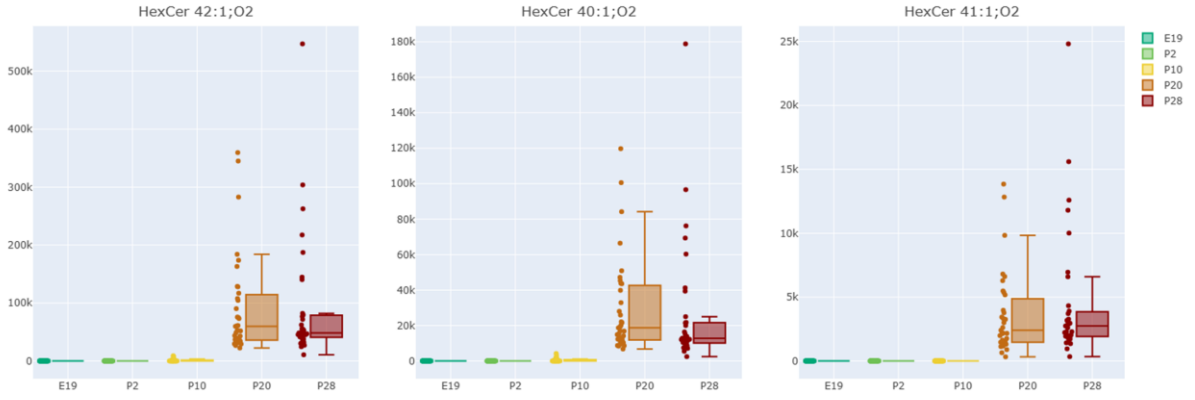

Fig. S8 Profiles of hexosylceramides in mPFC based on developmental stage. Metabolites were selected based on PLS-DA with a VIP score>1.